Università degli Studi di Padova

Department of Information Engineering

Master's Degree Course in Bioengineering

Quantification of [^{18}F]FDG kinetic parameters using an image-derive input function and integration with resting-state fMRI metrics

Supervisor:

Prof.ssa Alessandra Bertoldo

Co-supervisor:

Dott. Tommaso Volpi

Candidate:

Mattia De Francisci

Academic year 2021/2022

Abstract

Metabolic demand associated with resting-state brain activity is one of the main focus of neuroscience research. Task-free brain activation has been found to exhibit coherent spatial patterns, and the associated glucose consumption is predominant if compared to task activation. However, a complete characterization of the link between energy and function in the brain is still missing. The aim of this thesis project was to explore novel strategies for the integration between metabolic measures coming from Positron Emission Tomography based on fluorodeoxyglucose ([^{18}F]FDG PET) and functional information extracted from resting-state Functional Magnetic Resonance Imaging (rsfMRI) measures. This was done adopting two different perspectives. On one hand, it was verified how metabolic and functional networks, inferred from time-series correlation across brain regions, relate to each other. On the other hand, across-subject similarity between sets of metabolic parameters and functional features was assessed.
The analysis was performed on a dataset provided by Washington University in St.Louis, consisting of non-simultaneous PET and MR acquisitions on a large cohort of subjects.
A first part of the work focused on [^{18}F]FDG data. An Image-derived input function (IDIF) was extracted from the internal carotid arteries. This was later used for microparameter estimation with Variational Bayesian approach. Across-subjects correlation matrices were obtained for subjects series of K_1 and k_3 values. Moreover, average metabolic connectivity matrix was extracted from [^{18}F]FDG parcel-level TACs. Similarly, from fMRI data, average functional connectivity matrix was extracted. Regional Homogeneity (ReHo) and Global Functional Connectivity (GFC) were estimated and across-subjects connectivity matrices were obtained for both parameters.
Time-series connectivity matrices coming from both PET and fMRI images were used to assess similarity between metabolic and functional networks, whereas across-subject connectivity matrices were used to compare metabolic and functional parameters. To agevolate comparison, embedding was used on both time-series and across-subjects connectivity: this was based on application of a gaussian kernel, followed by calculation of the Laplacian Eigenmaps, a nonlinear dimensionality reduction techinque. Resulting manifolds are called *gradients* in neuroscience, and are commonly used to study functional architecture in the brain.
From a network perspective, metabolic and functional gradients exhibited sig-

nificant correlation, and the regions in which they overlapped the most belong to visual and sensorimotor networks. Similar results were found between all combinations of [^{18}F]FDG microparameters and fMRI features gradients, implying that both local and global functional relationship in the brain may be associated with specific metabolic fingerprints.

Contents

List of Figures

Chapter 1

Introduction

1.1 Brain metabolism and function

Energy utilization in the brain has been the focus of many studies, with the aim of understanding mechanisms underlying cognition and ageing, or to derive biomarkers for specific diseases, which could have an important role both in disease prevention and in the improvement of medical care for patients. The three key components in brain metabolism are represented by glucose, oxygen and blood flow, which can be respectively expressed as the cerebral metabolic rate of glucose ($CMRglc$), cerebral metabolic rate of oxygen ($CMRO_2$) and cerebral blood flow (CBF).
It seems that most of the energy delivered to the brain is used by neurons in order to restore resting membrane potential through the ATP-consuming activity of the ionic-pumps. It is believed that energy utilization is higher in regions richer in synapses [29] and it is reasonable to think that activation of neurons population is linked with increased regional energy consumption [5]. However, glucose utilization in synapses is not straightforward: according to the astrocyte-neuron lactate shuttle (ANLS) hypothesis [39], brain metabolism is regulated by an interplay between neurons and astrocytes. In brief, glucose can be metabolized through different metabolic pathways: after conversion to pyruvate through glycolysis, which produces small amounts of energy in the form of 2 ATPs, it can be completely oxidated through the tricarboxylic acid (TCA) cycle, with production of up to 36 ATPs (the entire reaction is indicated as *oxidative phosphorylation*), or, under low oxygen levels, pyruvate can be converted to lactate by lactate dehydrogenase enzyme through a process known as anaerobic glycolysis. When conversion to lactate happens in the presence of oxygen, the process is referred to as aerobic glycolysis. Oxidative phosphorylation and aerobic glycolysis are differently expressed in neurons and astrocytes, with astrocytes being more involved in production of lactate rather than the full oxidative pathway, that is predominant in neurons, as shown by related gene expression data. Following the release of glutamate, which is the main

neurotransmitter for excitatory synapses in central nervous system (CNS), non oxidative glucose utilization and glucose uptake from circulation is triggered in astrocytes. This brings to the production of lactate, which is in turn shuttled to neurons, where it can be further processed through the oxidative steps of the TCA cycle. The complexity of this mechanism is reflected on the interpretation of brain metabolism measures. In particular, increases in CBF and $CMRglc$ in response to a task or stimulus have been observed to be much higher than changes in oxygen consumption [28].
Measuring quantities such as $CMRglc$, $CMRO_2$ and CBF and unveiling their mutual relationships can advance our understading of brain metabolism and function. Over the years, PET scans have been extensively used for this purpose, since they can provide direct measures of all three components. More recently, there has been a growing interest in interpreting the blood-oxygenation level dependent (BOLD) signal measured in fMRI, which is strongly affected by $CMRO_2$ and CBF, together with cerebral blood volume CBV. If calibrated, fMRI can even provide measurments of $CMRO_2$ changes [13]. Although imaging of the brain through PET or fMRI is not a direct measure of neural activity in brain regions, since the recorded signals are not immediately linked to action potential in neurons, as it is the case of electrophysiological signals, these modalities are still useful to further investigate coupling between metabolism and function. However, the integration of the information coming from PET and fMRI data is still under continous investigation. A review of the two techiques is presented in following sections.

1.2 PET quantification

1.2.1 PET: physical principles and data acquisition

Positron emission tomography (PET) has proved to be an important neuroimaging tool, used both in clinics and in research. Its applications rely on the use of several radiolabelled ligands (or tracers), which produce a detectable signal. Tracers radioactivity is given by the presence of energetically unstable isotopes, which decay emitting a positron that in turn annihilates with an electron, producing two γ rays, emitted at 180-degree to each other. Detection of two opposite rays indicates that an annihilation event occurred along the detectors coincidence line, otherwise known as Line Of Response (LOR). Scintillation crystals in the gamma cameras (devices which the PET scanners are equipped with) convert the γ photons into light photons, with signal intensity dependent on the distance between detectors and source. Detectors provide radioactivity counts, that need to be translated into a 3D image using reconstruction algorithms.
One of the most common algorithms employed in PET images reconstruction is Filtered Back Projection (FBP), a modified version of the traditional back projection approach. In the latter, the different 1D acquired projections, relative to different angles, are spatially combined. However, the resulting image

appears blurred: representation of an object in the image can be seen as a convolution of the object itself and the so called Point Spread Function (PSF), thus determining the blurring of the object. To overcome this issue, in FBP a filter is applied to each of the projections. However, as a consquence of filtering (usually achieved by applying a ramp filter in the Fourier domain), the reconstructed image may be affected by noise, which can in turn leads to the presence of negative artifacts [43].
More recently, an iterative approach, based on maximum-likelihood expectation maximization (MLEM) has been proposed, known as Ordered-Subset expectation maximization (OSEM). As suggested by the name, scanner detectors are divided into subsets, and to each of these expectation maximization is applied, based on an initial estimate of the image. Division into subsets is introduced to accelerate convergence, and it does so by a factor proportional to the number of subsets [23]. In this case, differently from the FBP, the solution is bound to be non negative. However, computational burden may be an obstacle to the application of this algorithm.

During a PET exam session, the tracer is administerd intravenously, so that the radioactive substance can reach the organs traveling through the bloodstream: interaction between ligands and target regions can thus be visualized and quantified thanks to the use of the PET scanner, together with the subsequent processing of the images obtained. Different kinds of radioligands were developed to track physiological or pathological processes in the brain [32]. Depending on the experimental frameworks, it is possible to distinguish between static and dynamic PET studies. The first modality consists of a single-frame acquistion and is used mostly in clinical applications, whereas the second, being more expensive and complex, is preferred in research and requires multi-frame acquistions [7].

1.2.2 PET kinetic modeling

In order to derive quantitative information from dynamic PET, compartmental modeling is employed, a strategy based on a mathematical model which describes the physiological processes involved in the tracer kinetics. Each compartment is, by definition, an amount of well-mixed and kinetically homogenous material, and it is associated with a first-order time-dependent differential equation. The parameters of interest can be derived by using nonlinear estimators, such as Weighted Non-Linar Least Square (WNLLS)[9, 7]. The employed model varies with the radiotracer and the related physiological assumptions, and so does the number of parameters to estimate.

[^{18}F]FDG

One of the most commonly used radioligands is [^{18}F]fluorodeoxyglucose ([^{18}F]FDG). As a glucose analogue, it is usually preferred to [^{11}C]Glucose, which would be the ideal tracer for studying glucose kinetics, but, unlike [^{18}F]FDG, it produces

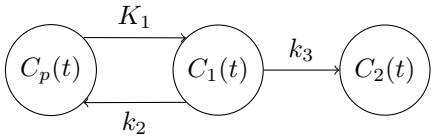

Figure 1.1: The 3K model

metabolites that need to be accounted for, leading to more complex models for studying its pharmacokinetics[9]. The compartmental model employed for [^{18}F]FDG, known as three-rate constants compartmental model (3K), was first presented by Sokoloff in 1977 and originally developed for 2-[^{14}C]deoxyglucose [47]. It is represented in 1.1.

In this model, $C_p(t)$ represents [^{18}F]FDG plasma arterial concentration, $C_1(t)$ the [^{18} F]FDG tissue concentration, whereas $C_2(t)$ is $[^{18}F]FDG$-6-P trapped in the tissue, i.e. the amount of radiotracer which underwent phosphorylation catalyzed by the enzyme hexokinase. Similarly, the associated rate constants K_1, k_2 and k_3 in equation 1.1 are respectively associated with the forward and reverse transcapillary membrane transport and the phosphorylation reaction. It is worth noticing that, once phosphorylation occurs, the tracer cannot go back to the previous form, and so the passage between the two compartments $C_1(t)$ and $C_2(t)$ is unidirectional. In other words, the tracer is trapped in compartment $C_2(t)$: such a compartment is said to be irreversible.

$$\begin{aligned} \dot{C}_1(t) &= K_1 C_p(t) - (k_2 + k_3) C_1(t) \quad & C_1(0) &= 0 \\ \dot{C}_2(t) &= k_3 C_2(t) & C_2(0) &= 0 \end{aligned} \tag{1.1}$$

After injection, the total concentration of radiotracer in the tissues, $C_t(t)$, is given by equation 1.2 (the so called measurement equation), which also accounts for the fraction of blood volume, V_b, and the related radioactivity concentration, $C_b(t)$ [9].

$$C_t(t) = (1 - V_b)(C_1(t) + C_2(t)) + V_b C_b(t) \tag{1.2}$$

The rate constants K_1, k_2 and k_3 can be estimated from PET images either at voxel level or at Region-Of-Interest (ROI) level. However, using conventional nonlinear estimators at voxel level may be ineffective due to the low signal-to-noise ratio (SNR). To overcome this issue, a Variational Bayesian approach has been proposed [10], which was applied in this thesis project. Alternatively, model macroparameters (i.e. combination of microparameters) result to be sufficiently informative in some cases: these can be estimated more easily by applying some transformation to the data that make it possible to use linear estimators. In particular, for [^{18}F]FDG PET studies, Patlak's method was developed [38], which works under the assumption that at least one compartment is irreversible, as it is the case of 3K model, leading to the estimation of K_i, which is the fractional [^{18}F]FDG uptake (see 1.3).

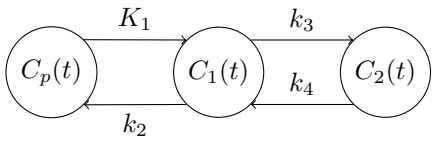

Figure 1.2: The 4K model

$$K_i = \frac{K_1 k_3}{k_2 + k_3} \tag{1.3}$$

Once, K_i is known, it is possible to derive the cerebral metabolic rate of glucose ($CMRglc$), by using a correction factor, the so called Lumped Constant (LC), which describes the relationship between the tracer and glucose itself. LC value is tissue dependent.

$$CMRglc = K_i \frac{C_{p-g}}{LC} \tag{1.4}$$

In equation 1.4, C_{p-g} indicates the subject's glycemia, measured at the beginning of the PET session.
It was noticed that, if the experiment lasts more than 120 minutes, radioactivity starts to fall down, as a consequence of the dephosphorylation of [^{18}F]FDG-6-P. For this reason, in 1979 Phelps and colleagues [41] proposed a modification of the 3K model by incorporating an additional rate constant, k_4, that accounts for dephosphorylation, thus making the second compartment reversible (see figure 1.2).

1.2.3 Input function

As already stated, quantification by means of compartmental model requires the assessment of an input function, and so arterial plasma radioactive concentration needs to be estimated throughout the dynamic acquistion. This is usually achieved by drawing arterial blood samples, a procedure which has many drawbacks. First of all, it may cause discomfort to the patients and expose them to risks of injuries and, in some serious cases, to artherial thrombosis [21]. Furthermore, technical personnel involved in collecting the samples is exposed to radiations. Finally, processing of the samples depends on some laboratory procedures, which may sensibly rise the costs associated with the dynamic acquisitions, preventing its translation to clinical practice. In brief, once samples have been drawn, radioactivity in blood, $C_b(t)$, is measured with a gamma counter. Plasma is then separated from blood cells through centrifugation, from which total radiactivity in plasma $C_{tot}(t)$ is measured by the gamma counter. For tracers which produce radiometabolites, plasma parent fraction (PPf, i.e. the fraction of radiactivity given only by the unchanged compound) needs to be estimated through high-performance liquid chromatography (HPLC), so that $C_p(t)$ can be obtained: this is the quantity directly fed to the model as a forcing

function, whereas $C_b(t)$ is necessary for blood volume correction, as shown in equation 1.2 [54].

IDIF

In the last decades, many efforts have been made to develop alternatives to arterial blood sampling, which still remains the gold standard procedure, despite its invasiveness and complexity. One promising approach is to derive the input function directly from the PET scans, exploiting the fact that some vascular structures are included in the FOV of the images. Most of these methods aims at extracting time-activity curves from internal carotids, either by defining an adequate ROI in the image or by exploiting some statistical techniques like Independent Component Analysis [64]. One of the most problematic issues involved with image-derive input function (IDIF) is relative to the limited resolution of the scanner and the small vascular caliber of the internal carotids: this results in spill-in or spillover, i.e. activity physically coming from surrounding tissues and accidentally mapped to the vessels area in the image, and spill-out, that is when the activity originating from smaller structures is distributed across sorrounding voxels [63]. Of course these factors need to be taken into account when dealing with IDIF. In modern scanners, where the FOV was expanded to include also the neck area of the subject, common carotid arteries, that have bigger caliber compared to internal carotid arteries, may represent a more robust alternative, since they should be less subject to spillover. Another possibility, yet to be validated, is represented by venous vessels [45].
Since the acquisitions analyzed for this thesis come from an old scanner (Siemens ECAT EXACT HR+) whose FOV exclude the area of the common carotids, we focused on the approaches based on internal carotid arteries (ICAs) ROI identification. In particular, we adopted the method proposed by Chen in 1998 [11] and validated for [^{18}F]FDG studies. Such a method is based on the segmentation of a ROI over the internal carotid arteries, identified on the early PET frames: more specifically, the summed images over the early 36-second period is used to identify arterial territory in the images, since this is the time when activity is around its peak in arteries and still very low in tissues. In addition to carotid segmentation, a tissue ROI is defined in proximity to the carotid ROI, identified by using the last PET frame superimposed over the early summed image. This last segmentation is used to perform spillover correction, together with a reduced blood sampling procedure consisting only of 5 venous samples, usually collected during the last 15 minutes, i.e. when the arteriovenous equilibration has been reached (so venous samples can be considered equivalent to the arterial samples)[63]. This correction is based on the assumption that $C_{mea}(t)$, which is the activity obtained from the carotid ROI, is given by a linear combination of the real plasma radioactivity $C_p(t)$ and the radioactivity spilled from the sorrounding tissue $C_t(t)$, measured from the tissue ROI.

$$C_{mea}(t) = RC \times C_p(t) + SP \times C_t(t) \tag{1.5}$$

In equation 1.5, RC stands for recovery coefficient, whereas SP is the

spillover coefficient from tissues to vessels.
It is worth emphasizing that the protocol described above is not entirely blood-free, as it still requires blood sampling. However, samples are reduced in number since they are collected only in the last 15 minutes of the PET session, and are drawn from veins rather than from arteries, so the precedure is less invasive and risky than the gold standard. Some completely blood free alternatives have been studied, but they still have some limitations and may bring to insufficient spillover correction, which has consequences on the subsequent kinetic parameters estimation, and especially on the microparameters [63]. With some tracers, one of the obstacle to IDIF employment is the need to estimate PPf. However, this is not the case for [^{18}F]FDG, which doesn't have any radiometabolites, as already mentioned.

Input function modeling

One important assumption for feeding input function to the compartmental model is that its time activity curve is noise-free. Of course this is not immediatly true for the measured plasma radioactive concentration, whichever the modality used to obtain it. A possible solution is to apply a model-based denoising. A physiological model, based on a compartmental description of the plasma input function and derived assuming a bolus injection of the tracer, was proposed by Feng and colleagues in 1993 [15], and it is reported below.

$$C_p(t) = \begin{cases} 0 & t < t_0 \\ A_1(t-t_0) + \sum_{t=1}^{3} A_i(e^{-a_i(t-t_0)} - e^{-a_1(t-t_0)}) & t \geq t_0 \end{cases} \tag{1.6}$$

In equation 1.6, t_0 indicates the injection time. A modification of this model is reported in 1.7, accounting for the fact that injection is not instantaneous.

$$C_p(t) = \begin{cases} 0 & t < t_0 \\ \frac{\sum_{t=1}^{3} A_i}{t_{peak} - t_0}(t-t_0) & t_0 \leq t < t_{peak} \\ \sum_{t=1}^{3} A_i e^{-a_i(t-t_{peak})} & t \geq t_{peak} \end{cases} \tag{1.7}$$

In equation 1.7, t_0 indicates the time of the injection of the radiotracer, whereas t_{peak} indicates the input function peak time. This model describes the three phases that are expected from radioactivity concentration in plasma, which are a zero phase (before the injection), a fast rising phase, here modeled as a straight line, and finally an exponential-like clearance, that can be approximated as a tri-exponential curve, with each of the three a_i accounting for different velocities in the decay [53].

1.2.4 Microparameters estimation: Variational Bayesian approach

As already stated, using WNLLS approach at voxel-level wouldn't provide reliable parameter estimates due to the low SNR. A solution is provided by the Variational Bayesian approach, which has been adapted to PET data in [10]. Exploiting Bayes theorem, it is possible to obtain the posterior parameters distribution $P(\Theta|y)$ starting from expectations on parameters values, formalized as prior distribution $P(\Theta)$, where Θ is the parameters vector and y are the observed data:

$$P(\Theta|y) = \frac{P(y|\Theta)P(\Theta)}{P(y)} \tag{1.8}$$

As shown in 1.8, calculation is based on knowledge of the so called likelihood $P(y|\Theta)$. However, in real applications, deriving integrals for the posterior calculation is unfeasible, and so it is necessary to resort to an approximation of the real posterior. In this case, computational burden is shifted to finding the best approximation, that is equivalent to minimizing the distance between real posterior and the approximated form $Q(\Theta)$. Such a distance is expressed as Kullback-Leibler divergence (KL):

$$KL[Q(\Theta)||P(\Theta|y)] = logP(y) - F \tag{1.9}$$

Since $logP(y)$ does not depend on Θ and KL is always non-negative, minimizing KL is equivalent to maximizing free energy F:

$$F = \int Q(\Theta) log \frac{P(y|\Theta)P(\Theta)}{P(y)} d\Theta \tag{1.10}$$

A possible solution for $Q(\Theta)$ is represented by the *mean field approximation*, obtained separating Θ into two groups, one comprising model parameters θ and the other relative to noise parameters ϕ. In [10], a multivariate normal distribution (MVN) for θ and a Gamma distribution (Ga) for ϕ are assumed. The priors, which are based on the same models as the approximated posteriors, are estimated directly from data. In practice, ROI-level WNLLS is first used, and the derived parameters estimations are propagated along all the ROI voxels as priors. ROIs definiton, which is crucial for priors distribution derivation, is usually based on pre-existing brain atlases or, alternatively, data-driven clustering can be employed to divide time-series in homogeneous groups.

1.2.5 Metabolic connectivity

A recent approach applied to PET dynamic studies is represented by metabolic connectivity. The term was coined by Lee and colleagues [27], indicating the adoption of a network perspective in the analysis of [^{18}F]FDG data, with the intent of characterizing relationships between metabolic measurments in different brain regions. This is usually carried out through multivariate statistical techniques applied to *subject series* of [^{18}F]FDG parameters. The techniques

usually employed include Seed Correlation Analysis, Independent Component Analysis, Principal Component analysis (PCA), Sparse inverse covariance estimation (SICE) and Graph theory [60]. These were mostly applied to series of standardized uptake value (SUV) or $CMRglc$ [57]. For this thesis project, the approach was extended to the analysis of microparameters K_1 and k_3.
A different investigation modality for metabolic connectivity can be derived operating in a similar manner as with Functional Connectivity (FC), and so computing inter-regional correlation directly from time-series data. However, just a few examples of this kind of approach on PET data are available [52, 1]. One of the most problematic issue with using PET time-series is represented by the impact of multicollinearity, which calls for an adequate standardization approach [59]. A possible solution is discussed in paragraph 2.2.3, and used to derive time-series metabolic connectivity in this work.

1.3 fMRI functional connectivity

1.3.1 MR scanner: physical principles

Magnetic Resonance (MR) scanner functioning is based on the application of magnetic fields using several electromagnetic coils, in combination with Radio Frequency (RF) pulses. Its use in medical imaging exploits the composition of human body, which is mostly made up of water. When exposed to the effects of a static magnetic field, B_0, spin magnetic moments associated with hydrogen nuclei in water molecules become aligned with the magnetic field direction. As a consequence, spins of the different atoms, that usually have random direction, become parallel, thus generating a non-zero net magnetization vector M. When a transient magnetic field (usually a RF energy), B_1, is applied in addition to the B_0, a phenomenon known as nuclear magnetic resonance (NMR) happens, which is the target of the MR scanner. It is in fact possible to deviate the magnetization vector so that the component M_z in the direction z of the static magnetic field disappears, in favor of a component M_{xy} in the perpendicular xy-plane. Once excitation with B_1 stops, M_z is recovered with a velocity that depends on tissue composition: time to reach equilibrium is called T_1 relaxation time, and this generates the so called T_1-weighted images. M_{xy} relaxation time T_2 is always less or equal than T_1 and depends on molecular interactions. In non ideal condition, actual relaxation time in xy, referred to as T_2*, is also affected by dishomogeneities in B_0: this generates T_2*-weighted images.
In 3D space, application of B_0 along z direction makes it possible to excite a confined slice, where frequency and phase encoding are used to appropriately map the two remaining directions. By acting on repetition time (TR), which is the time between two consecutive RF pulses, and echo time (TE), so the time between the beginning of the RF pulse and the instant of its maximum intensity, it is possible to obtain different kind of sequences. Among these, Echo Planar Imaging (EPI) sequence allows to obtain T_2*-weighted images with improved temporal resolution, making it feasible to follow dynamic processes, as in fMRI.

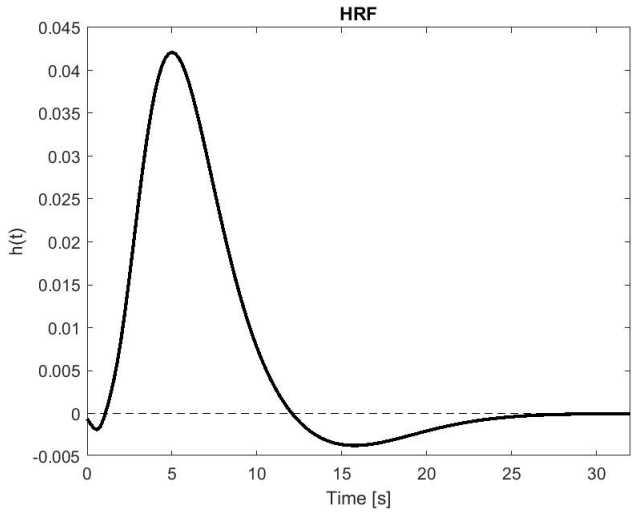

Figure 1.3: Hemodynamic response function

1.3.2 fMRI and BOLD signal

Functional magnetic resonance is the biomedical imaging technique employed for monitoring brain activity through the use of the MR scanner. Experiments led by Ogawa and colleagues in 1990 [35] showed for the first time MRI potentiality to measure blood oxygenation by exploiting hemoglobin as an endogenous contrast agent. Deoxygenated hemoglobin (deoxyhemoglobin) is in fact paramagnetic, and as a consequence it interferes with magnetic excitation of tissues, causing a decrease in T_2* relaxation time. On the contrary, oxygenated haemoglobin (oxyhemoglobin) is diamagnetic, so signal intensity increases when its concentration is higher than the deoxygenated counterpart. This signal is known as BOLD (blood oxygenation level dependent) and it is an indirect measure of neuronal activation. As already discussed (see 1.1), regional energy demand in the brain involves the activity of both neurons and astrocytes. Whenever a region is activated, a cascade of events is triggered, such as new capillaries recruitment and vasodilation. This determines an increase in both cerebral blood flow (CBF) and cerebral blood volume (CBV). Since oxygen consumption is delayed with respect to activation (glycolytic step in astrocytes precedes oxidative metabolic path in neurons), oxyhemoglobin accumulates in proximity to the activation area, causing an increase in signal intensity. BOLD signal is indeed strictly linked to the hemodynamic response function (HRF): according to the interpretation provided by Friston and colleagueas [17], HRF serves as a low pass convolution filter for neural activity, which gives rise the the measured BOLD signal. Looking at 1.3, it can be observed that HRF presents an undershoot, probably caused by the fact that, once activation phase in neurons population ends, CBF decreases faster than CBV, so deoxyhemoglobin level are even higher than the baseline level (before activation). It can also be

noticed that in HRF there's an initial dip, whose physiological meaning is still debated. Interestingly, similar pattern can be observed in measures of lactate levels, and so initial dip in BOLD can be interpreted as a result of the early activation of the oxidative pathway in neurons through conversion of lactate shuttled from astrocytes [29].
Possibility of measurement of the BOLD signal relies on some technical requirements. First of all, a magnetic field strength greater than or equal to 1.5 T is needed. Another important parameter is represented by TR: considering that HRF has a duration of around 10 seconds, a TR at least equal to 2 seconds is needed to reconstruct the entire signal from samples without any information loss.

1.3.3 Resting state fMRI

Since the introduction of fMRI, its most immediate application has been the investigation of brain activity induced by external stimuli or tasks performed by the subject inside the scanner: this approach is known as task-fMRI. However, the idea that intrinsic task-free brain activity could be meaningful had already emerged in previous studies. From the metabolic perspective, during the [^{18}F]FDG PET experiments led by Sokoloff in 1955, no change in glucose consumption was detected between the resting state condition and a situation where the subject was involved in solving a complex arithmetical problem [48]. This was probably due to the fact that the change was too small to be detected by the available tools, as it was later shown that a moderate increase in energy consumption actually occurred during task [16]. From these first results, it was possible to conclude that, even when the brain is considered at *rest*, and so when subject is not involved in activities other than thinking, metabolic demand is still significant and actually predominant.
Initially, resting state BOLD signal constituted the baseline to which task induced activation patterns were compared, and its slow ($< 0.1\ Hz$) fluctuations were treated as noise [46]. A change in perspective happened when coherent patterns of resting state activation were first observed within the somatomotor system [8]. From that time on, studying brain functioning in resting state has become one of the priorities in neuroscience research, both for the sake of understanding more about the meaning of these intrinsic activations, and for finding new leads in brain diseases research.

Functional Connectivity and brain networks

Resting-state Functional Connectivity (FC) was developed with the intent of characterizing intrinsic brain activity by finding regions which show mutual coherence in signal fluctuations. Application of this techinque led to progressively describe brain functional architecture. According to similarity and synchronization in low-frequency fluctuations, several brain networks have been identified in the last years. A functional organization of cerebral cortex was derived by Yeo and colleagues in 2011 [61], confirming definitions of networks that had been

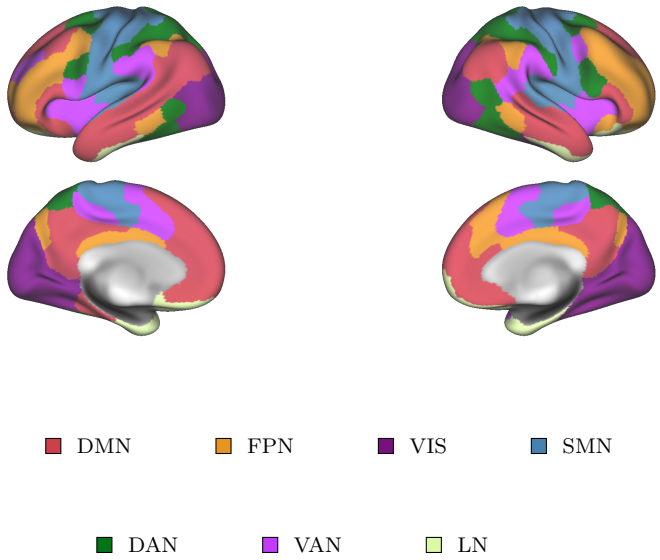

Figure 1.4: Yeo's 7 networks represented over Schaefer's parcellation

previously presented. In particular, based on FC profiles, cortical regions were clustered in 7 distinct networks: Default-Mode network (DMN), Ventral attention network (VAN), Dorsal attention network (DAN), Visual network (VIS), Frontoparietal network (FPN), SomatoMotor network (SMN) and Limbic (LN) (see figure 1.4). Among these, VIS and SMN are mostly confined to specific sensory and motor cortices, whereas the remaining networks span across different association regions. In particular, DMN is a task-negative network: this means that it tends to be less active during task than during rest. Interestingly, this unique feature was first reported in PET studies, when decrease in blood flow was observed in certain areas during visual task activation [44]. Anatomical regions comprised in DMN are the medial prefrontal cortex, precuneus area and angular gyrus. Its function is still debated, but it appears to be involved in activity such as mind wandering, autobiographical memory or thinking about the future. The idea of two separate attention networks was first proposed in 2002 [12], with DAN devoted to voluntary reorientering of attention and VAN activated in response to unexpected stimuli. VIS network is located on the occipital lobe, an area that had already emerged as responsible for processing visual stimuli in task-fMRI studies. Similarly, motor and somatomotor cortices functionality, included in the SMN, had been long studied even before the advent of fMRI. FPN is located along the lateral prefrontal cortex and anterior inferior parietal lobule, areas involved in cognitive control [26] and working memory [34]. What is referred in Yeo's networks organization as *limbic* lies mostly on the orbitofrontal cortex and temporal poles. Its role is still debated: it has been joined to FPN in some studies [55], whereas in parcellation proposed by Gordon and

colleagues in 2016 [19] these regions have been included into a *None* network, as the areas with low FC not clustering within any other network. Clustering activity coming from *limbic* areas is indeed problematic due to the distortions in the signals caused by magnetic susceptibility changes between tissue and air. Moreover, a recent study investigating BOLD signal variability between regions using multi-echo fMRI, has associated *limbic* activity with DMN [4].

It is worth considering that networks organization delineated by Yeo and later reproduced with some minor differences in Schaefer functional atlas [42], although being very influential, is not universal. One of the most debated aspect in neuroscience is the number of networks in which the entire brain architecture can be decomposed [55]. Same study by Yeo [61] also proposes a division of the main networks in 17 distinctive subnetworks, based on the stability of the derived clusters. Different networks classification have been presented over the years and, although it appears that there is not a definitive or right answer, the need for a consensus has been expressed [55].

Another useful FC parameter for measuring similarity within neighborhood of nodes (intended as voxels or vertices) is represented by *Regional Homogeneity* (ReHo), [62]:

$$W = \frac{\sum(R_i)^2 - n(\overline{R})^2}{\frac{1}{12}K^2(n^3 - n)} \tag{1.11}$$

In equation 1.11, W is the *Kendall's coefficient of concordance* (KCC), K is the number of nodes in the neighborhood, R_i is the rank of the i_{th} time point, $\overline{R}$ is the mean of the ranks and n the number of time points in each time-series. When specific regions are activated, ReHo in involved parcels is expected to increase, thus yielding information about the localisaiton of brain functions.

Adopting a different perspective, it is also useful to characterize level of integration of each node with all the others. For this reason, Global Functional Connectivity (GFC) was recently introduced as a complementary fMRI feature. In order to calculate GFC, for each voxel or region, the average correlation between its time-series and all the others is computed [2].

1.4 Connectivity Gradients

Exploring topography of brain features has always been a trending topic in neuroscience. Derivation of structural and functional gradients across the brain cortex (and even subcortex [50]) is an emerging modality to respond to this need. Gradients constitute sets of axis along which brain regions are represented in relation to specific features, such as histology or function. They are obtained through embedding of brain data to a space where similar nodes end up being close to each other. Differently from parcellation, which divide brain regions by delineation of discrete spatial boundaries, gradients offers the possibility to represent gradual change in the examined features [3].

An important result from gradients analysis applied to resting state fMRI data came in 2016 from Margulies and colleagues [31]: decomposition of connectivity matrices revealed a principal gradient in which DMN lies at the opposite end of primary sensory and motor regions. This actually confirmed what was previously postulated by Mesulam [33]: a synaptic hierarchy emerged from his tractracing studies of the macaque monkey, with different synaptic levels involved in cognition, starting from primary sensory and unimodal zones, up to the association areas represented by hetero-modal, paralimbic and limbic regions. Consistency between the two studies served as a validation of gradients use in neuroscience community. As a result, in the last years, gradients have been extensively exploited in research. An interesting potentiality offered by gradients is the integration between different imaging modalities of brain data: this has been done for example between fMRI and microstructural data [36]. As far as we know, gradients were never used to integrate [^{18}F]FDG PET and fMRI data. This was attempted in this thesis project as a new strategy for investigating the relationship between metabolism and function.

1.4.1 Mathematical derivation of gradients

The core of gradients derivation methods is usually represented by a dimensionality reduction technique. Among these, it is possible to distinguish between linear and non linear approaches. A commonly used linear solution is provided by principal component analysis (PCA), which outputs gradients as principal directions of variation. In case of non linear approach to dimensionality reduction, gradients are to be intended as *manifolds* rather than directions. These techniques have the potential to disentagle complex geometrical relationships between data points in the original space. Two algorithms used in literature are Laplacian Eigenmaps (LE) and Diffusion Mapping (DM). Starting from a graph representation, LE reproject data into a new space where nodes are grouped together based on their similarity. DM operates in a similar manner, but it models probability of transition from a node to the other.
Independently from the dimensionality reduction solution adopted, the input data should be represented by a symmetrical matrix. This is usually assured by the application of a kernel function, such as cosine similarity, gaussian kernel, or simply Pearson's correlation.
To sum up, gradients derivation methods usually comprise two main steps: 1) calculation of an affinity matrix based on some kernel function, 2) application of a dimensionality reduction technique.
For functional gradients, input data is usually represented by connectivity matrices: so what is expected from reprojecting data points (usually brain parcels) into the new space is that connected nodes end up being close to each other. Functional connectivity matrices are usually obtained by applying Pearson's correlation, and, since they are already symmetrical, it would be sufficient to apply the dimensionality reduction technique of choice directly to the input data, without resorting to any further similarity kernel. This is equivalent to the application of the entire gradients derivation pipeline (made up of the two

steps presented above) to time-series data, using Pearson's correlation as an affinity measure. However, starting from symmetrical correlation matrices, it has been also attempted to apply an additional kernel function, such as cosine similarity or gaussian kernel, before dimensionality reduction, with positive effects on reliability of the results obtained [22].

Laplacian Eigenmaps

For this thesis project, Laplacian Eigenmaps was chosen to perform the embedding required for gradients derivation. This algorithm has been shown to be robust in the face of non-linear relationships [20], and its reliability is comparable to PCA [22].
As anticipated, LE is a non linear dimensionality reduction technique which starts from a graph representation of data. Given an affinity matrix A, the associated graph is made up of interconnected nodes, whose edges are weighted according to reciprocal similarity, as calculated by the kernel function. Using the affinity matrix, graph Laplacian L is calculated:

$$L = D - A \tag{1.12}$$

In equation 1.12, D is the diagonal degree matrix, whose elements are defined as $D(i,j) = \sum_j A(i,j)$. L is, by construction, a matrix with rank equal to $n-1$ (with n indicating the number of nodes). Once L is calculated, the generalized eigenvalue problem in equation 1.13 is solved.

$$L\mathbf{g} = \lambda D\mathbf{g} \tag{1.13}$$

The eigenvectos $\mathbf{g} = [g_1, g_2, ..., g_n]$ represent the manifolds for the new embedding. Differently from other dimensionality reduction techniques such as PCA, in LE most informative eigenvectors are associated with the smallest eigenvalues, and so, to select a subset of $m < n$ eigenvectors, eigenvalues are to be sorted in ascending order. However, the first smallest eigenvalue is always equal to 0, and it is associated with a constant eigenvector, which is always a solution of the laplacian eigenvalue problem (since L is singular). Considering that the constant eigenvector wouldn't express any variance in the original data, it is normally discarded. Moreover, the second smallest eigenvalue can be taken as a measure of how well connected the graph is, and it is known as *algebraic connectivity* [3]. It can be shown that solving 1.13 is equivalent to the minimization of a cost function represented by the distance of the nodes in the new space:

$$U(x) = \sum_{ij} W_{ij}(x_i - x_j)^2 \tag{1.14}$$

W_{ij} are the weights in the graph, and so the similarity measure computed between node i and j. Minimizing 1.13 implies that data points, once projected in the new space, will be close to each other if they are strongly connected in the graph (i.e. similar in the original space). In case of fMRI time-series, this

means that regions which show similar connectivity fingerprints will be grouped together in the new space.

Chapter 2

Materials and methods

2.1 Dataset description

2.1.1 [^{18}F]FDG PET data

Dynamic acquisitions (60 min) from 71 cognitively unimpaired individuals (56±15 years old) on a HR+ PET scanner were provided by Washington University community (St Louis, MO, USA). Subjects received a [^{18}F]FDG bolus (185 MBq). For most subjects, dynamic reconstruction grid consisted of: 24x5s, 9x20s, 10x60s and 9x300s frames (see figure 2.2). Two different reconstruction algorithms were applied: filtered back-projection (FBP) and ordered subset expectation maximization (OSEM). For this thesis work, most of the analysis was performed on FBP reconstructed images, apart from MC matrix derivation.
During PET dynamic acquisitions, venous samples were collected for 55 subjects from the antecubital vein, with different sampling schedules: for most of the subjects sampling occured 5, 10, 15, 20, 30, 45 minutes after the injection of the radiotracer, whereas for a minority of subjects only three samples were acquired, after 30, 40 and 50 minutes. Each sample consisted of about 2 ml, half of which was used to measure radioactivity in plasma. Radioactivity counter measurements was given in counts per 12 seconds. The counter's efficiency (0.2707 cps/Becquerels) was experimentally determined.

2.1.2 MRI data

For the same cohort of individuals who underwent PET dynamic acquistions, MRI data were separately acquired on a Siemens Prisma 3T scanner. For each subject, Multi-echo T1w MPRAGE was provided, (TR=2500,TI=1000 ms, TE=1.81, 3.6, 5.39, 7.18 ms, voxel size=0.8 x 0.8 x 0.8 mm). Alternating anterior-posterior (AP) and posterior-anterior (PA) phase encoding, 4 rsfMRI runs (AP, PA, AP, PA), each on consisting of 375 volumes acquired over 5 minutes, were recorded as Gradient-Echo Multi-Band images (TR/TE=800/33 ms, flip angle=52°, voxel size=2.4 x 2.4 x 2.4mm, MultiBand factor=6), together

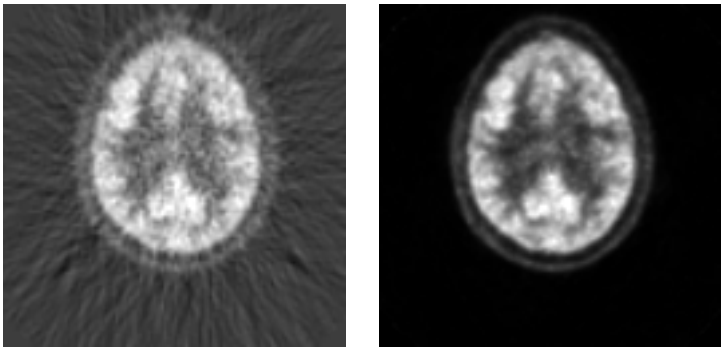

(a) FBP (b) OSEM

Figure 2.1: Axial slice from images reconstructed by the two different algorithms

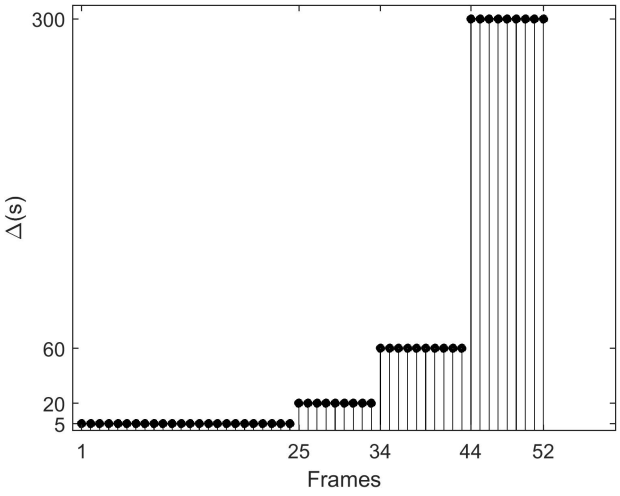

Figure 2.2: PET reconstruction time grid

with 2 Spin-Echo (TR/TE=6000/60 ms, flip angle= 90°) sequences acquired with opposing polarities of the phase-encode blips for image distortion correction.

Structural preprocessing

Preprocessing was performed on T1w images, which were later used to coregister both PET and fMRI data. T1w images were bias field corrected using ANTs' N4, skull stripped using ANTs' BrainExtraction tool and segmented into gray matter (GM), white matter (WM), and cerebrospinal fluid (CSF), using SPM.

2.2 [18F]FDG data analysis

2.2.1 IDIF extraction

In order to proceed with micro and macro-parameters estimation for each subject, it was crucial to obtain a robust estimation of arterial plasma radioactivity to use as input function to the compartmental model. To this purpose, we implemented a revisitation of Chen original approach [11] for deriving the input function from the internal carotid arteries (ICA) and correcting for spillover. In particular, our implementation differs from the procedure originally proposed by Chen and colleagues since ICA and tissues segmentations are performed automatically by our algorithm and just require tuning of some parameters. Moreover, before averaging the TACs derived from the selected ROIs, a voxels selection procedure based on k-means parametric clustering is applied to time-series. Finally, a tri-exponential model based on [15] is fitted against the data to obtain a noise-free input function, before applying Chen's correction. Details about these procedures are illustrated in the following paragraphs.

Carotids segmentation

To obtain segmentations of the carotids, we decided not to use time-of-flight (TOF) angiography since 1) it was not available for all the subjects, 2) it would require coregistration to the PET images, which could result in misaligned ROIs. However, a vessels image was still necessary to guide the ROI selection, and so we generated a pseudo-TOF by summing the first PET frames, taking into consideration the fact that in the first minutes of the acquisition tissue radioactivity is still negligible and most of the contribution to the signal is given by tracer concentration in vessels. This approach was adapted from [11], with an important variation: rather than imposing a rigid time threshold (36 seconds in the original paper) to limit the number of frames included in the sum, we used an individualised threshold for each subject, dependent on the estimation of the arterial $C_p(t)$ peak time. This choice is motivated by the significant inter-subjects variability found in arterial peak time, that made it impossible to find a threshold suitable for all the individuals. Moreover, using estimated arterial peak time as a threshold proved to be useful in reducing the visibility of veins

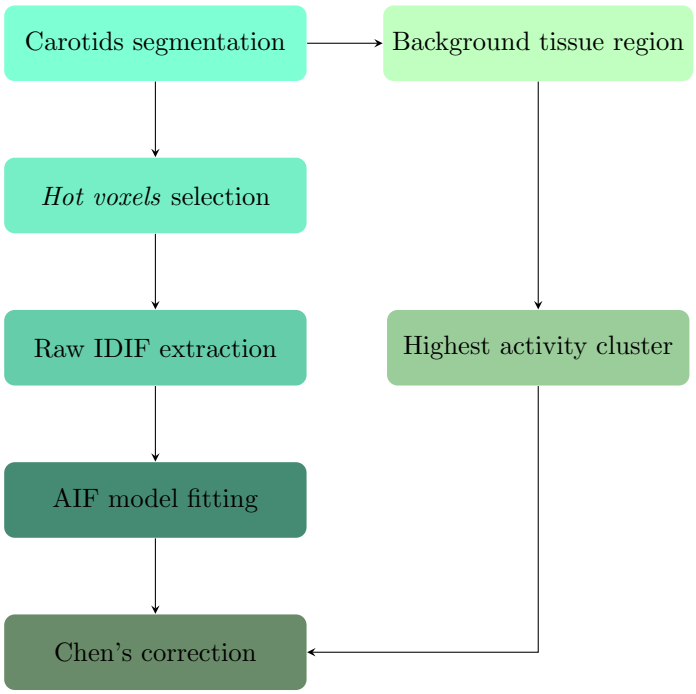

Figure 2.3: Pipeline for IDIF extraction

After carotid segmentation, 40 arterial voxels are selected and averaged to extract the raw IDIF. The curve is denoised through model fitting. Together with carotid segmentation, sorrounding tissue is segmented and highest activity region identified to later perform Chen's correction

in the pseudo-TOF, considering that venous peak is delayed with respect to arterial peak.

However, the estimation of arterial peak time was not trivial without first identifying ICA region: the strategy we adopted, considering time framing in our data, was to first identify venous peak frame, and then use the frame which immediately preceded it as a first approximation of arterial peak time. Venous peak time was found by summing PET frames (up to 60 seconds) and binarizing the resulting image, thus obtaining a mask which we will call *late pseudo-TOF*. For each TAC extracted from the *late pseudo-TOF*, peak time was calculated and the mode was taken as estimation of venous peak time, considering that the biggest vascular structures included in the FOV are represented by superior sagittal sinus (SSS) and transverse sinuses. This approach actually led, in many cases, to an overestimation of the arterial peak time, but it is still good enough to partially exclude contribution of venous vessels in the final pseudo-TOF image (referred to as *early pseudo-TOF*). Automatic segmentation was obtained by adapting the Hessian-based filter for enhancement of vascular structures implemented by Jerman and colleagues [25]. Since venous sinuses are not completely absent in the early pseudo-TOF, before applying the algorithm a masking procedure has been devised to constrain the search of the *vesselness* algorithm to a subspace in the volume. With the aim of creating this search box, a subset of slices was automatically selected for each plane of the volumetric scan. First of all, to obtain a 3D image that better highlighted brain anatomy, the last 10 frames were summed. Then, a maximum intenisty projection to each of the three planes (axial, sagittal, coronal) was calculated, and from this, summing again along one of the two remaining planes, a one dimensional signal was obtained. Then, taking into consideration brain shape, thresholds based on percentiles of the 1D final projections were calculated. For both coronal and sagittal planes, same threshold (70^{th} percentile) was used for identifying upper and lower bounds of the subset of slices. Since 1D projection in axial plane was not symmetrical and the aim was to exclude the area of the SSS (above) and the background (below), 30^{th} and 80^{th} percentiles were chosen as upper and lower bounds. The final box is generated from the intersection of the slices selected from each plane. The entire procedure is summarized in figure 2.4.

The output of the Jerman filter consists of a vesselness probability map, which we binarized by adjusting a threshold iteratively, up to the inclusion of an adequate number of voxels (around 500), so that the ICAs were correctly marked. Additional clean up is performed by selecting the two biggest connected 3D structures (that are expected to be the internal carotid arteries). The entire segmentation algorithm was first run with default parameters, set for all the subjects in the dataset. Each output segmentation was then visually inspected and some were repeated, if considered unsatisfactory, using parameters individualised for the specific subjects.

Simultaneously with internal carotids segmentation, background region for spillover correction has been derived by morphological dilation of the vessels mask. This approach was adapted from [49]. In order to identify the most

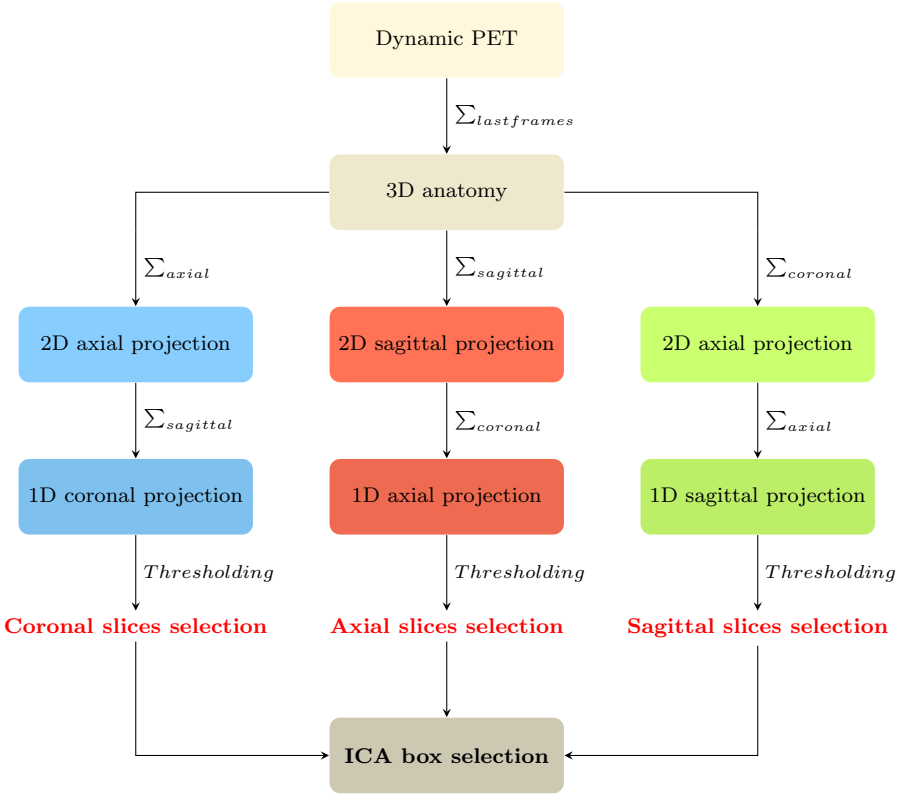

Figure 2.4: ICA box selection procedure

For each of the three planes, a 2D projection is obtained and then reduced to a monodimensional signal whose shape depends on brain profile. Thresholds based on each monodimensional projection provides a subset of slice. Intersection between the three subsets provides the final box in which ICAs can be segmented

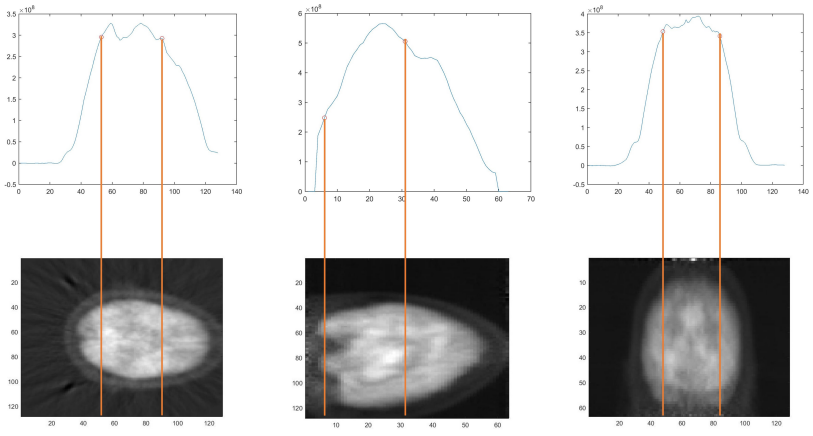

(a) coronal slices selection (b) axial slices selection (c) sagittal slices selection

Figure 2.5: Slice selection procedure for the three planes

It can be observed how coronal and sagittal cuts are provided by symmetrical percentiles, whereas for axial cut thresholds are not symmetrical: the intent is to exclude area of the SSS from above and background area from below

appropriate tissue region to perform correction, two concentric masks were generated: a first one, around ICAs, which is probably the most affected by spill-out activity from vessels, and a second, built around the first, which is the one actually used for correction. Both these masks have internal radius equal to twice the voxel size, i.e. around 5 mm (see figure 2.6).
Once the background mask was obtained, related voxels TACs were extracted. k-means (K=3, replicates=1000, distance= squared Euclidean) was applied on late frames (from around 30 minutes), the cluster with highest activity was then selected and its centroid (median of all the TACs in the cluster) adopted as a first raw approximation of the real $C_t(t)$.

IDIF modelling

Since many voxels in the mask are affected by sorrounding tissue activity, associated TACs present lower peaks than expected or higher tail, and so they are not good candidates for representing radiactivity in plasma. Average of the entire pool of TACs derived from the mask would provide a $C_p(t)$ with underestimated peak amplitude, which can be critical in terms of microparameters estimates. To overcome this potential problem, a *hot voxels* selection step based on [40] has been implemented. First, peak time is caculated for each TAC, then global peak time is estimated as the mode of all individual peaks time and all the voxels whose peak is not synchronized with the estimated peak time are discarded. A second selection is based on parametric k-means clustering (K=2, replicates=500, distance=squared Euclidean), applied to all the time-series sur-

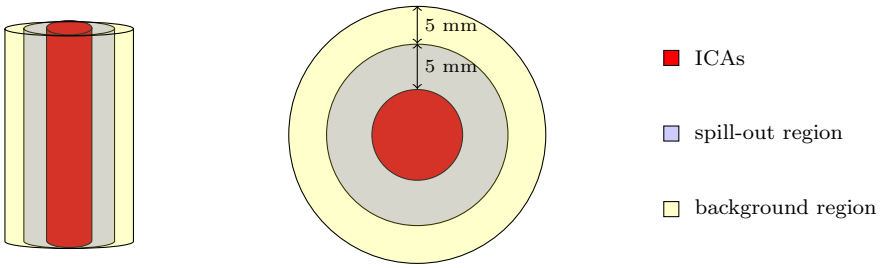

Figure 2.6: Background region

In order to automatically segment the tissue region for performing Chen's correction, two concentric cylinders are built around the ICAs mask. The first cylinder reprsent the spill-out region, which is affected by ICAs activity, whereas the background region is the tissue area which is expected to affect ICAs activity

viving the first step of selection, based on calculation of parameters such as peak amplitude, tail mean value, rising slope, ending slope, AUC before peak, AUC after peak, standard deviation. The cluster whose centroid show the highest peak is selected, and associated time-series are sorted by peak height: the first 40 voxels, i.e. with highest peak, are kept and averaged to obtain the raw IDIF.

Considering that time framing is very dense in the beginning and data tend to be really noisy, time-series have been partially undersampled. In particular, starting from peak time, for all the remaining 5 seconds frames, sparser sampling is obtained by averaging data points in 15 seconds time windows.

Final denoising is obtained by fitting model 1.7 against undersampled time-series. For the non-linear part of the model WNLLS has been first used to fit the three exponential decays. Weights were determined by employing the typical noise model for PET studies [6], which consists in a non-identity covariance matrix Σ_e, where each diagonal elements is obtained as $\Sigma_e(t_i, t_i) = y(t_i)/\Delta_{t_i}$, with $y(t_i)$ indicating the measurement at time t_i and Δ_{t_i} equal to the duration of i^{th} time frame. Non diagonal elements are set to 0, since noise is supposed to be uncorrelated. Σ_e is built accounting for the fact that PET data are acquired over time frames of different lenghts, and so noise level is not equal for all data points.
With respect mostly to the slowest exponentials, fitting was not satisfactory for many subjects in terms of coefficient of variation CV (higher than 100%), so a pool of well-fitted curves was selected, and averages of each parameter (exponential decays a_1, a_2, a_3 and amplitudes A_2 and A_3) were used as priors for a MAP estimation applied to all subjects (adapted from [56]). For the linear part of the model, i.e. the straight line that represent the rising phase of the $C_p(t)$, two different approaches have been tested: 1) Linear Least Squares (LLS) has been applied to fit the slope, 2) original unfitted values have been used.

Chen's correction

Model in equation 1.5 was fitted against arterial denoised curves using a LLS estimator for the subjects whose venous samples were available. The last three decay corrected venous samples were used as $C_p(t)$, whereas the first samples, that had been drawn before arteriovenous equilibrium time, were not used. The radioactivity counter measurements, provided in counts per 12 seconds, were converted in counts per seconds (cps). Radioactivity measures were also normalized by plasma sample weight into radiactivity concentrations (kBq/ml). The following formula was applied for decay correction:

$$A_t = A_0 2^{-\frac{t}{T_{1/2}}} \tag{2.1}$$

where A_t is radioactivity measured by the counter, A_0 is radiactivity when the sample was drawn from the subject vein and $T_{1/2}$ is the halflife of the radioisotope (109.8 min for [^{18}F]FDG). $C_t(t)$ from tissue mask and $C_{mea}(t)$ from ICA mask were interpolated to the venous sampling time-grid. Estimated RC and SP were then used with original $C_{mea}(t)$ and $C_t(t)$ to calculate corrected $C_p(t)$.

2.2.2 Microparameters estimation: Variational Bayesian approach

VB approach adapted to PET data analysis, as implemented in [10] (see 1.2.4), was used to derive voxel-wise estimates of K_1, k_2, k_3 and Vb using corrected IDIF. To proceed with estimation, some preprocessing steps were required. First, last 9 frames (from 44^{th} to 52^{th}), whose acquisition windows last 5 minutes, were motion corrected using an in-house combination of PMOD (www.pmod.com) and *FSL mcflirt* [24], with 44^{th} frame employed as target for the alignment of the subsequent frames. Same pool of frames, after motion correction, was used to derive a pseudo-static PET, later coregistered to T1w preprocessed image using ANTs. ROIs for priors derivation were identified by applying k-means (k=11, replicates=500, distance=squared Euclidean) clustering on TACs: in particular, a total of 11 clusters were obtained, 6 of which for GM and 6 for WM (exploiting segmentations obtained by structural preprocessing, see 2.1.2). Prior variance λ was set to 0.5, which is the optimal value identified through simulated data in [10]. Finally, parameters maps are brought to MNI space using ANTs so that voxelwise group average can be calculated for each parameter map.

2.2.3 Metabolic connectivity

Time-series

Time-series metabolic connectivity (MC) matrices are derived for each subject as in [60]. PET dynamic OSEM reconstructed images were employed. The choice of OSEM over FBP reconstruction was aimed at reducing impact of

noise on time-series, which could affect correlation results, especially for the first 25 frames, i.e. the ones acquired over 5 seconds windows. MC computation was performed over parcellated data. For cortical parcels derivation, Schafer functional multiresolution atlas was used: it is based on the 7 and 17 networks identified by Yeo [61], and it was released in several versions. For this study, the 200 parcels atlases for 7 and 17 networks were used. In addition to the 200 cortical parcels, 14 subcortical parcels were concatanated, corresponding to anatomical regions of thalamus, caudate, putamen, pallidum, hippocampus, amygdala and accumbens area, and derived from *FSL FIRST* subcortical atlas [37]. Parcels, originally in MNI space, were registered to T1w space and finally to PET space in order to derive related TACs.
Before computing pairwise correlation, parcels time-series were interpolated over a uniform denser time grid (step=1s). Normalization was then performed. Parcels time-series were first z-scored as follows:

$$X_{z2} = \frac{X_1 - \mu_p(t)}{\sigma_p(t)} \tag{2.2}$$

In the equation above, X_1 is the original data, X_{z2} are the time-series after zscoring along parcels, μ_p and σ_p are the mean and the standard deviation calculated along parcels, as in 2.3 and 2.4.

$$\mu_p(t) = \frac{1}{P}\sum_{p=1}^{P} X_1(p,t) \tag{2.3}$$

$$\sigma_p(t) = \sqrt{var(X_1(:,t))} \tag{2.4}$$

Secondly, mean of the z-scored data X_{z2} is calculated (equation 2.5) and subtracted to each parcel time-series (equation 2.6):

$$\mu_{X_{z2}}(p) = \frac{1}{T}\sum_{t=1}^{T} X_{z2}(p,t) \tag{2.5}$$

$$X_S = X_{z2} - \mu_{X_{z2}} \tag{2.6}$$

Normalization is necessary before computing correlation because of the collinearities of PET time-series. Finally, Pearson's correlations (see 2.7) between parcels normalized TACs (X_S) was calculated and stored in a 214x214 symmetrical matrix.

$$r_{xy} = \frac{\sum_{i=1}^{n}(x-\overline{x})(y-\overline{y})}{\sqrt[2]{\sum_{i=1}^{n}(x-\overline{x})^2}\sqrt[2]{\sum_{i=1}^{n}(y-\overline{y})^2}} \tag{2.7}$$

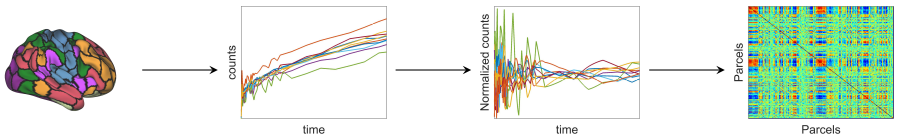

Figure 2.7: Time-series Metabolic Connectivity derivation

Procedure employed for deriving metabolic connectivity. After deriving parcels time-series from Schafer atlas, normalization is applied to reduce collinearities. Finally, correlation matrix is obtained through Pearson's coefficient calculation.

Subject-series

As done for time series, using the 200 Schaefer cortical atlas, for both 7 and 17 networks versions, and 14 FIRST subcortical parcels atlas, parameters values were extracted. Subjects-series of parcels parameters values were thus obtained as a 214x55 matrix. After z-scoring within subjects, Pearson's correlations between subject-series were calculated and 214x214 correlation matrices were obtained for both K_1 and k_3.

2.3 fMRI data analysis

The analyses were performed on the first AP run.

2.3.1 Preprocessing

The basic preprocessing steps for fMRI data were adapted from Human Connectome Project (HCP) minimal preprocessing pipeline[18]. First of all, slice timing was performed, followed by distortion correction using *FSL TOPUP* and based on the provided SPIN ECHO (SE) image for the specific phase encoding. Motion correction was then performed with *FSL's mcflirt*, using an EPI template (mean volume) as reference. Finally, functional data were coregistered to skull-stripped T1w structural image.
Additional preprocessing applied to fMRI were confound-regression and filtering. For the first operation, the contributions coming from motion parameters, their first order derivatives and the first 5 Principal Components (PCs) of WM and CSF were removed. A high pass filter (HPF, cut-off frequency=0.1 Hz) and a low pass filter (LPF, cut-off=0.1 Hz) were then applied in sequence to the regressed data. T1w and EPI image were both brought to MNI space.

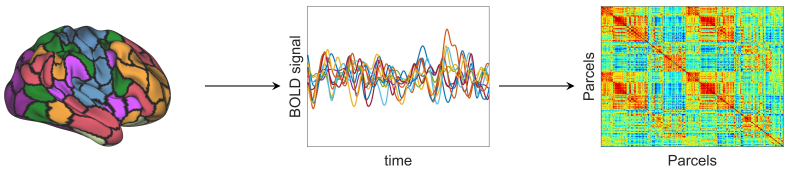

Figure 2.8: Functional Connectivity Derivation

Procedure for deriving functional connectivity. Starting from parcels time-series, Pearson's correlation is applied to obtain symmetrical FC matrices. Differently from MC, no normalization is required

2.3.2 FC and fMRI features computation

Time-series

For FC computation, volumes which showed a Framewise displacement (FwD) greater than 0.3 mm were discarded. Time-series related to the 200 cortical parcels from Schafer 7 networks atlas and 14 subcortical parcels derived using FLS FIRST (see paragraph for details) were extracted, averaging voxels time-series for each parcel. FC matrices (214x214) were derived for each subject applying Pearson's correlation to parcels time-series.

Subject-series

ReHo voxel-level maps were obtained, using the formula reported in 1.3.3, with number of voxels per neighbourhood set to 27. Similarly, GFC voxelwise map were also obtained. Then, using Schaefer cortical and FIRST subcortical atlases in EPI space (obtained by first coregistering from MNI space to T1w space and finally to EPI space), parcel-level ReHo and GFC estimates were derived. ReHo values coming from differents subjects were concatanated as column vectors in a single matrix (214x71), which was then z-scored within subjects. Correlations between each pair of ReHo subject-series were calculated and stored in a 214x214 matrix. The same was done for GFC.

2.4 Connectivity Gradients and PET-fMRI multimodal integration

2.4.1 Time-series analysis

This part of the analysis was performed on a pool of 22 subjects, for which both OSEM reconstructed PET images and fMRI data were available. Once FC and MC matrices were obtained, averages of both were calculated. Subjects who had less than 50% of uncensored volumes in processed rsfMRI time-series were discarded, and the resulting pool of individuals was used to calculate group-average matrices for the two modalities. Limbic regions were excluded, so that

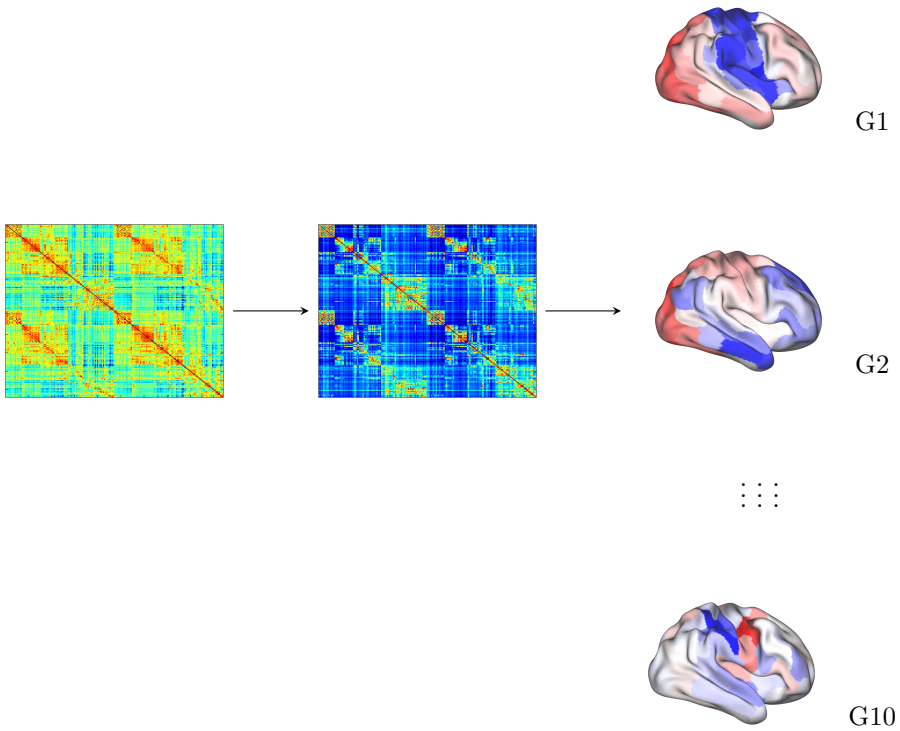

Figure 2.9: Gradients derivation procedure

Starting from an input matrix (a symmetrical correlation matrix in this case), gaussian kernel was applied in order to derive new *manifolds* for data representation

bias coming from AP phase encoding did not affect results, and also considering that limbic network functional distinction is still not clear. Subcortical parcels were also excluded to focus exclusively on cortical gradients. *BrainSpace* toolbox was employed [14] for gradients calculation. Row-wise sparsification of the input matrix, which ensures to have a connected graph for calculation of the Laplacian, was performed, keeping only values above 90th percentile. Results from using the original unsparsified data and the sparsified version were compared. Gaussian kernel was used to obtain final similarity matrix (see 2.8), followed by application of LE.

$$A(i,j) = e^{-(\gamma||x_i - x_j||^2)} \tag{2.8}$$

First 10 eigenvectors, sorted according to the associated eigenvalues importance (excluding the first, which is constant and so not informative), were calculated. Eigenvectors scores were represented over hemispheres using HCP Connectome Workbench [30] in order to provide gradient maps and to visual inspect results. Gradients scores were also grouped by networks to test capability of distinguishing them using the new manifolds. In order to integrate information from the two modalities, two approaches were tested. The first was the joint alignement of gradients, as implemented on the *BrainsSpace* toolbox. In brief, this is a variant of gradients calculation which attempts to project both the data matrices in a common space, using a joint similarity matrix J, which is built including intra-dataset (A_I) and inter-dataset (A_{IJ}) affinity matrices:

$$J = \begin{pmatrix} A_1 & A_{12} & \dots & A_{1N} \\ A_{12}^T & A_2 & \dots & A_{2N} \\ \vdots & \vdots & \ddots & \vdots \\ A_{1N}^T & A_{2N}^T & \dots & A_N \end{pmatrix} \tag{2.9}$$

Secondly, to test similarities between sets of gradients, masks were created in which best corresponding areas between gradients are marked. This was done using tails of the unaligned gradient scores distribution, keeping only 20% top and bottom values. Discrete masks were obtained for the two modalities, with top values represented as 1 and bottom as -1. These were combined, first by summing them without any transformation, and then by repeating the sum after inverting sign of MC discrete mask: this is necessary to compare unaligned gradients since reference can be flipped when space projection is performed separately for different matrices. Another possibility to overcome this issue is represented by Procrustes's alignement, but it had been verified that this procedure drastically changed the resulting MC gradients shape when using FC as reference. Between the two combinations obtained from each couple of discrete masks, the one with greatest number of non-zero parcels was kept, assuming that it was correspondant to the best overlap. This procedure has been repeated for all the combinations of the first two MC and FC gradients. To test overall gradients similarity, Pearson's correlation for each couple of gradients was also computed.

2.4.2 Subject-series analysis

This part of the analysis was limited to a pool of 45 subjects, for which both functional features and metabolic parameters had been calculated. For across-subjects covariation of [^{18}F]FDG K_1, k_3 and rsfMRI features, similarity matrices were calculated using gaussian kernel on sparsified (90th percentiles) and unsparsfied matrices, followed by application of LE. The same procedure for identification of best overlapping regions, which had been performed on time-series gradients, was also repeated for subjects-series gradients. Correlation between first two gradients coming from the subject-series of the different parameters were computed in order to assess similarities.

Chapter 3

Results

3.1 [^{18}F]FDG data analysis

3.1.1 IDIF extraction

Carotid segmentation

ICAs were automatically segmented for all subjects and then visually inspected. An example of ICAs segmentation mask is represented in figure 3.1. For most subjects, using default parameters for ICAs segmentation was successful. In a minority of cases automatic segmentation was considered unsatisfactory and it was repeated with individualized parameters. In particular, head positioning had an impact on the selection of the subset of slices which contain the carotids. For instance, if the head was sligthly bent to one side during acquistion, the threshold used to select the slices from the axial plane needed some adjustment. Similarly, if the head was positioned towards the bottom of the FOV, the number of slices which are masked out due to noise was reduced. Another parameter which needed tuning was the expected number of voxels in the final ICAs mask, which served as a threshold for binarizing the vesselness probability map, output of the Jerman Filter. For more details, see figure 3.2.
Together with segmentation of the carotid arteries, the tissue region to be used for Chen's correction was segmented. The three clusters grouping TACs extracted from the tissue mask had a consistent spatial organization across subjects, with the highest activity cluster collocated in the same area which was manually segmented in Chen's original paper [11](see figure 3.3).

IDIF modelling

Hot voxels selection through parametric clustering was used to identify the best candidate TACs for $C_p(t)$ extraction (see 3.4): in most cases, this procedure led to the identification of exactly 40 voxels, which was the maximum allowed. In a minority of cases, the surving time-series in the selected cluster were fewer than 40.

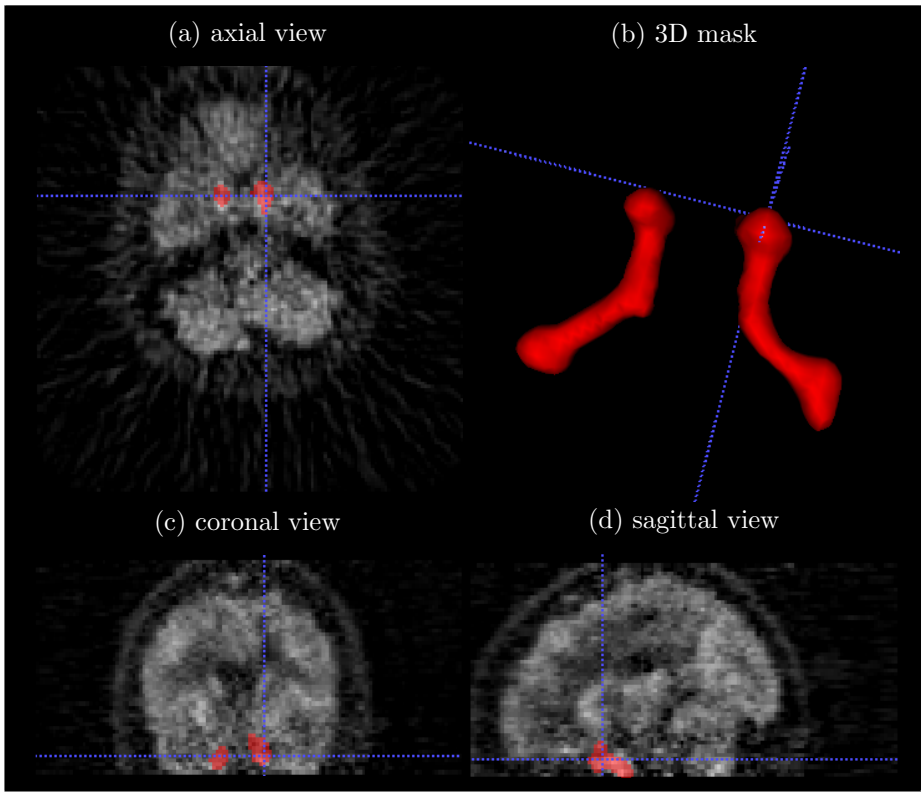

Figure 3.1: Carotid mask

Internal carotid arteries mask superimposed over average PET image

Undersampling the $C_p(t)$ proved to be efficient in reducing the noise, as shown in figure 3.5. However, it had little to no impact on the $C_p(t)$ obtained after tri-exponential model fitting (figure 3.6). The raw and fitted curves for all subjects are represented in figure 3.8. Even in cases when the raw IDIF was too noisy to obtain a good fit, MAP estimation using adequate priors was efficient enough to obtain a reliable $C_p(t)$ estimation (figure 3.7). Mean parameters relative to the fitted $C_p(t)$ are reported in table 3.1.
Fitting a straight line to the rising part of the IDIF (up to the peak) was compared to using the original raw curve. Using the raw curve preserves a smoother rising phase, even if the resulting IDIF may be affected by artifacts coming from the reconstruction time grid employed (see figure 3.9). This was the version finally used as input function for compartmental modelling.

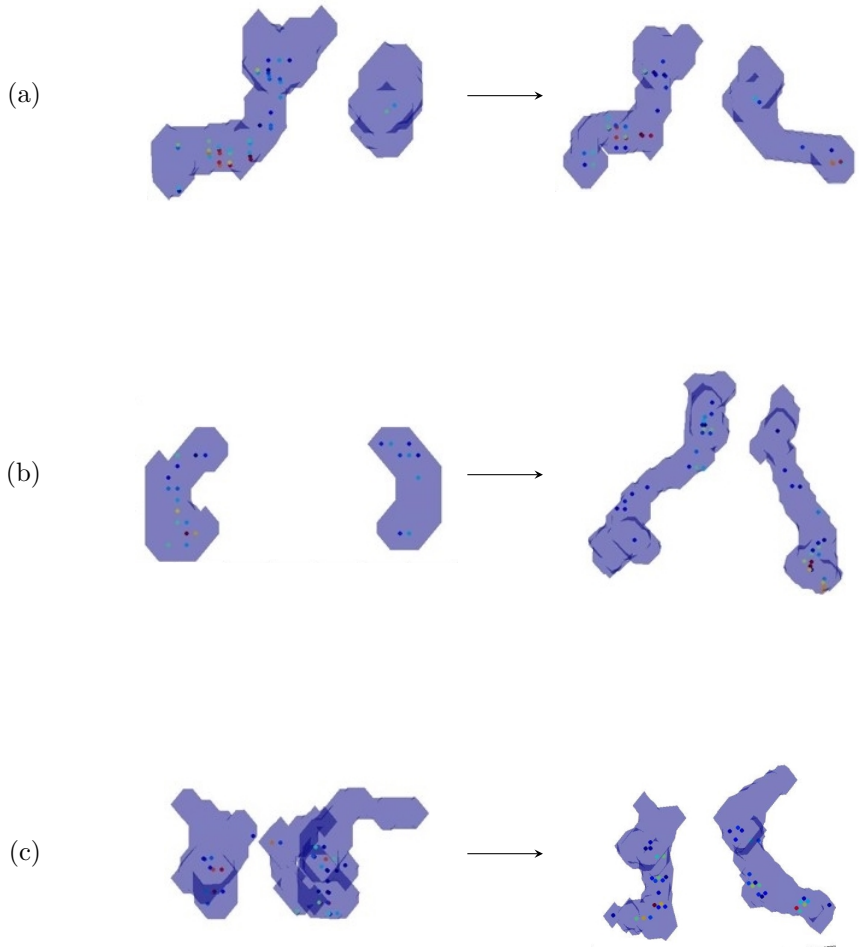

Figure 3.2: Tuning of segmentation parameters

Examples of segmentation corrected by manual tuning of algorithm parameters. (a) Subject head was bent to one side, resulting in asymmetrical ICAs mask: changing the thresholds for axial slices selection led to a symmetrical mask. (b)Subject head was positioned towards the bottom of the FOV: in order to obtain a complete segmentation of the carotid area, the number of axial slices that were masked out due to noise was reduced. (c) In this case the default value corresponding to the expected number of voxels, used for binarization of the vesselness probability map, was reduced to obtain a physiologically-plausible segmentation

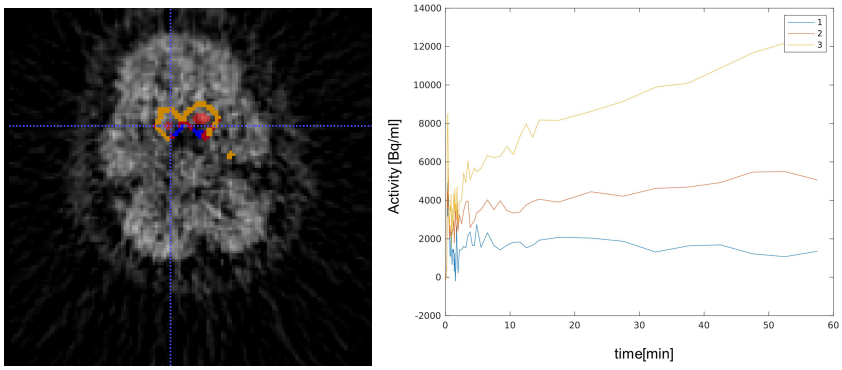

(a) (b)

Figure 3.3: Tissue mask for Chen's correction

(a) Background mask for Chen's correction superimposed on PET average mask and clustered into three regions (blue, orange, yellow),(b) Centroids(=median across TACs) from the three clusters

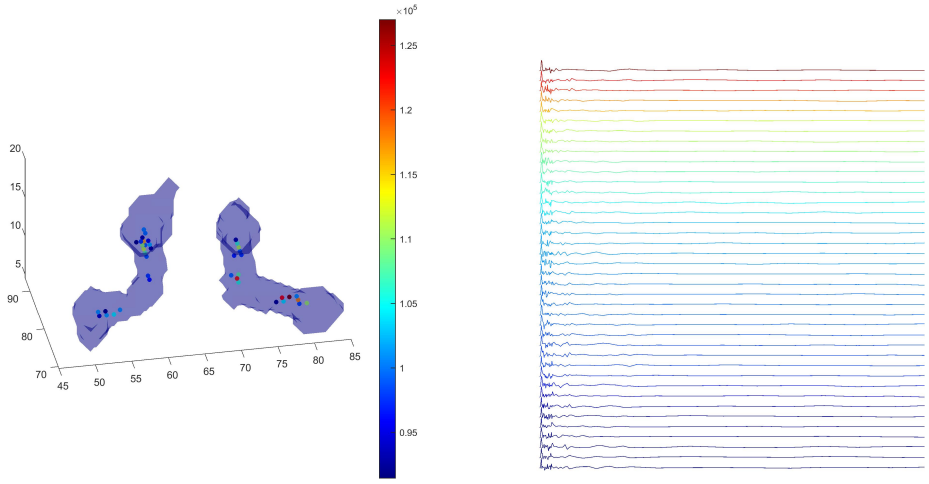

Figure 3.4: Arterial voxels selection from ICAs mask

On the left, ICAs mask is shown with the 40 voxels selected by parametric clustering, with corresponding peak amplitude as indicated by the colormap [Bq/ml]. On the right, the normalized TACs are shown, sorted by peak amplitude

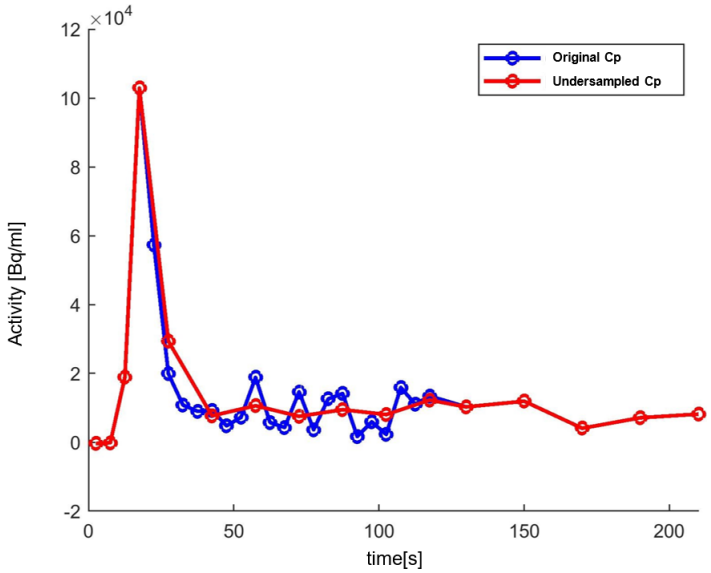

Figure 3.5: Undersampled $C_p(t)$

Using a 15 seconds frame sampling grid, noise impact is reduced for the first time points

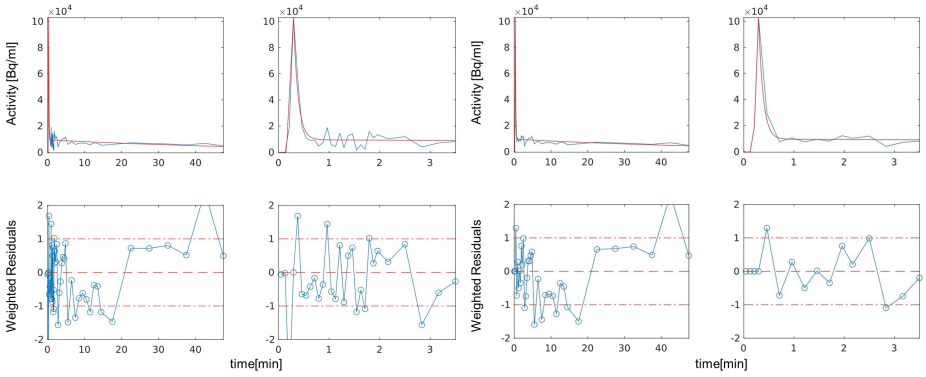

(a) (b)

Figure 3.6: IDIF model fitting

Triexponential model fitting results using original raw IDIF (a) and undersampled IDIF fitted without initial LLS (b)

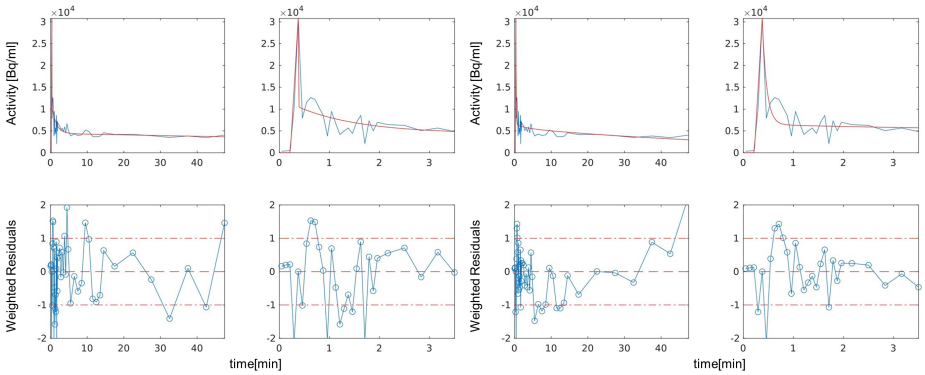

Figure 3.7: MAP estimation

Raw IDIF fitted using WNLLS (a) and using a MAP estimation approach (b). MAP estimation is robust even when the input curve is very noisy, leading to a physiological $C_p(t)$ estimate

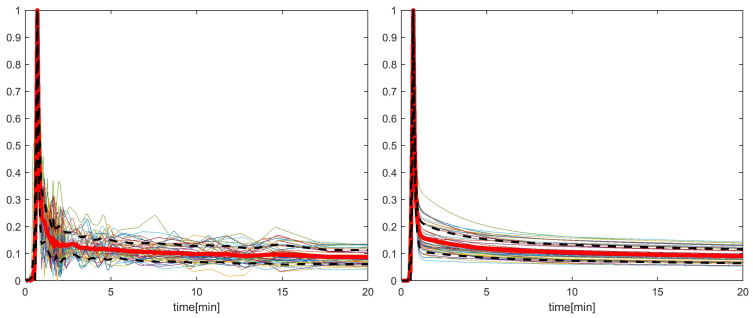

Figure 3.8: raw IDIF and fitted $C_p(t)$

Raw (a) and fitted (b) curves zoomed in the first 20 minutes. All curves were normalized and synchronized with respect to peak time. Average is shown in thick red, confidence intervals (mean + SD) in dotted black

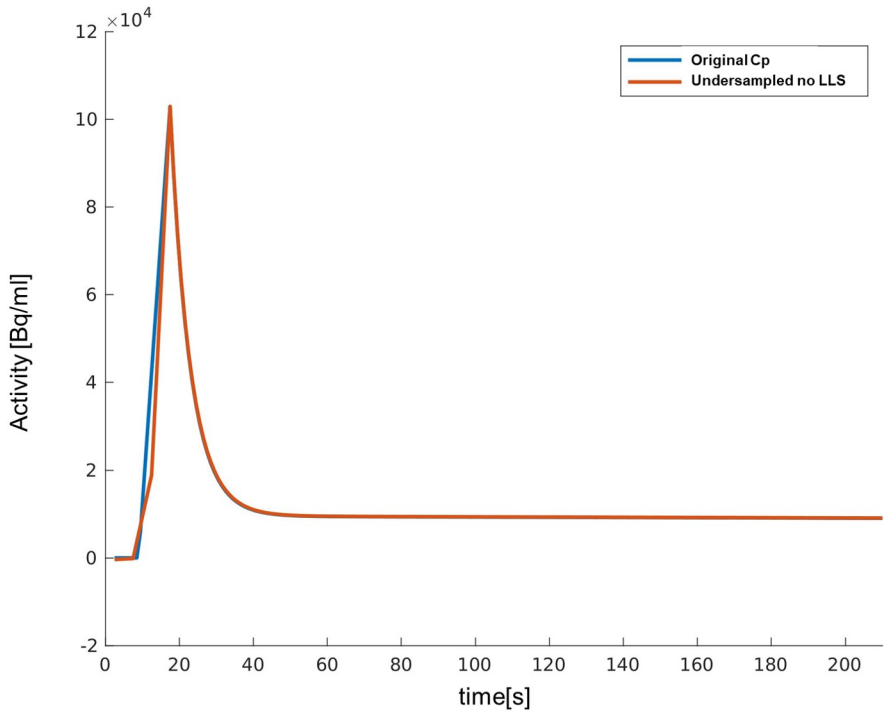

Figure 3.9: Straight line and raw curve for the rising phase of the IDIF

$C_p(t)$ obtained fitting a straight line to the rising part of the IDIF (up to the peak) is plotted in blue, whereas $C_p(t)$ obtained using the original raw curve for the initial part is plotted in red.

	MEAN±SD
time to peak [s]	24.75±6.7
peak amplitude [KBq/ml]	65±18.2
AUC [KBq*min/ml]	310±59.2
A_2/A_1 [unitless]	0.04±0.04
A_3/A_1 [unitless]	0.13±0.04
α_1 [min^{-1}]	11.01±0.25
α_2 [min^{-1}]	0.37±0.002
α_3 [min^{-1}]	(1.54±0.2) x 10^{-2}

Table 3.1: IDIF parameters

Chen's correction

Chen's correction was performed using available venous samples. The resulting $C_p(t)$ shows a more gradual decay than the uncorrected curve. In some cases, the tail of the corrected curve was scaled down becoming lower than the tail of the uncorrected version, probably when the spillover effect was predominant. As a consequence of rescaling using the estimated RC, peak amplitude was increased in the corrected $C_p(t)$. For more details, see figure 3.10.

3.1.2 Microparameters estimation: Variational Bayesian approach

The VB approach allowed to obtain voxel-wise estimates of K_1, k_2, k_3, V_b (and K_i as a macroparameter). The subject-level K_1 and k_3 and K_i parametric maps were normalized to MNI152 space, and their average and variability (CV%=SD/mean*100) across subjects were evaluated. The CV% maps show high consistency of parameter estimates across subjects, without significant regional heterogeneity (figures 3.11, 3.12, 3.13).

3.1.3 Metabolic Connectivity

Time-series

Time-series MC average matrix is shown in figure 3.14, where parcels are grouped based on Yeo's resting state networks. It can be noticed that typical within-network correlation usually present in FC matrix is also present in MC for the VIS network and for some parcels belonging to FPN. Moreover, VIS network activity is anticorrelated with parcels activities of the other six functional networks.

Subject-series

Across subjects correlation matrices for K_1 and k_3, parcelled using the Schaefer cortical and FIRST subcortical atlas (214 regions), were made sparse (90^{th} per-

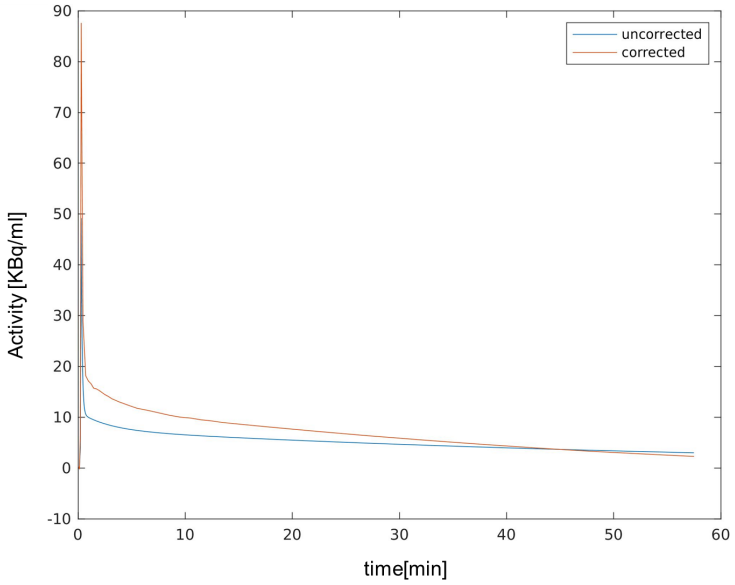

(a)

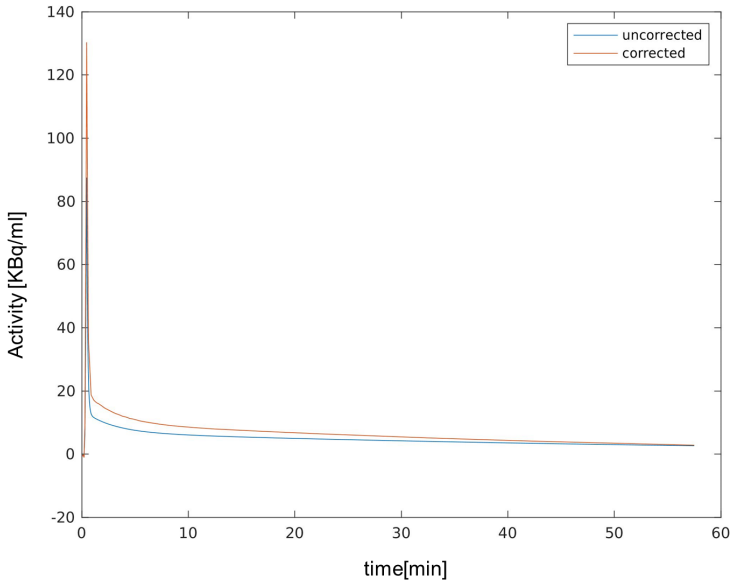

(b)

Figure 3.10: Chen's correction

In (a) the rescaled IDIF tail became lower than the uncorrected curve, whereas this does not happen in (b). However, decay becomes steeper as a consequence of Chen's correction, and peak higher

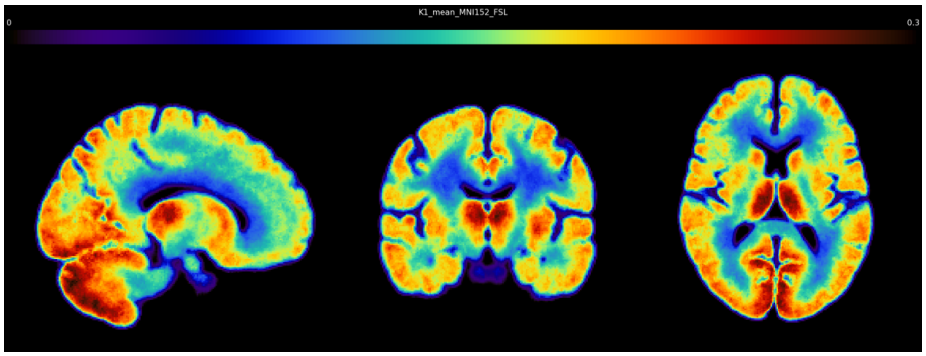

(a) K_1 [ml/cm^3/min]

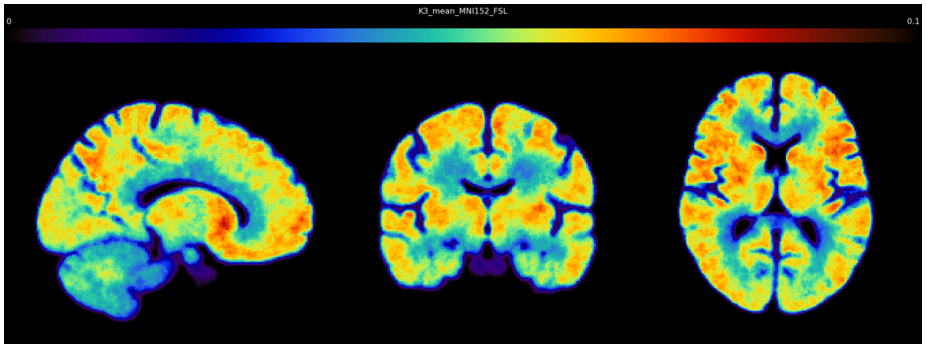

(b) k_3 [min^{-1}]

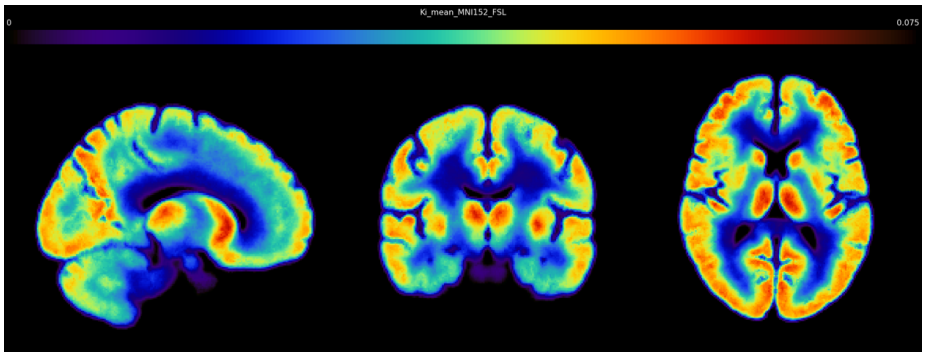

(c) K_i [ml/cm^3/min]

Figure 3.11: Microparameter average maps

Mean maps (across subjects) were obtained after coregistration of each individual parametric map to MNI space

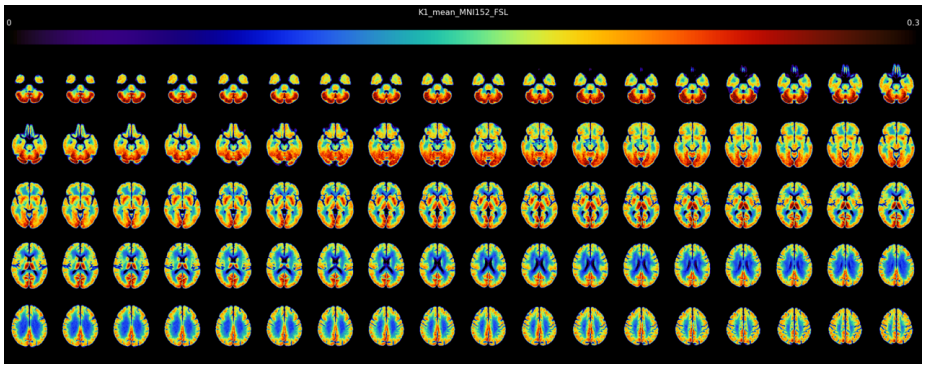

(a) K_1 [ml/cm^3/min]

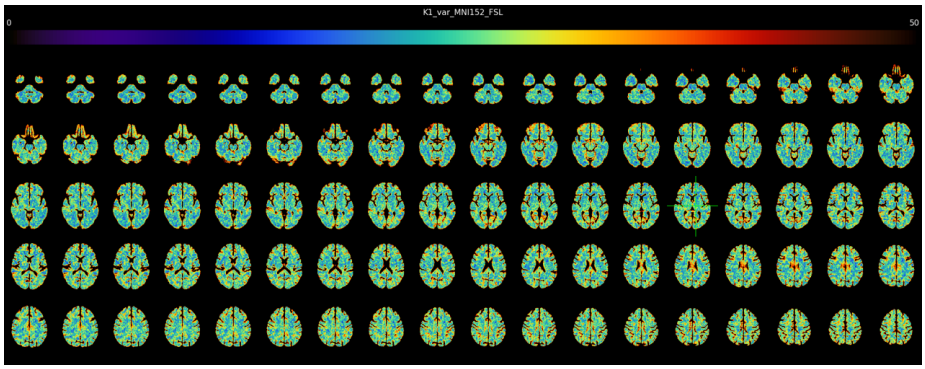

(b) K_1 CV%

Figure 3.12: K_1 average map and CV %

Multislice axial visualization of K_1 average across subjects and corresponding CV

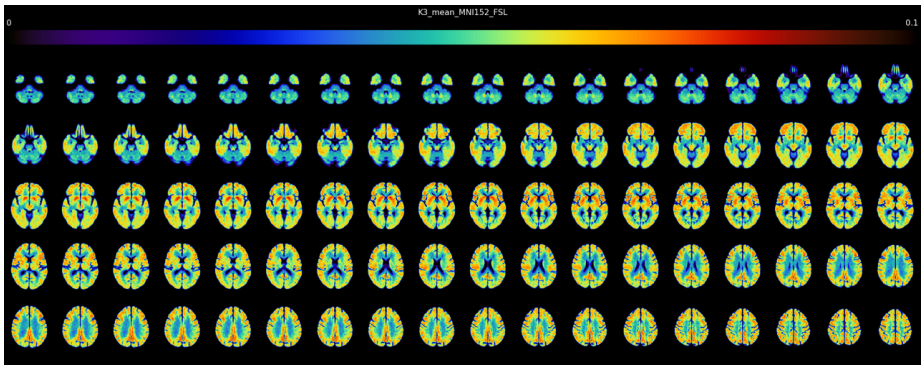

(a) k_3 [min^{-1}]

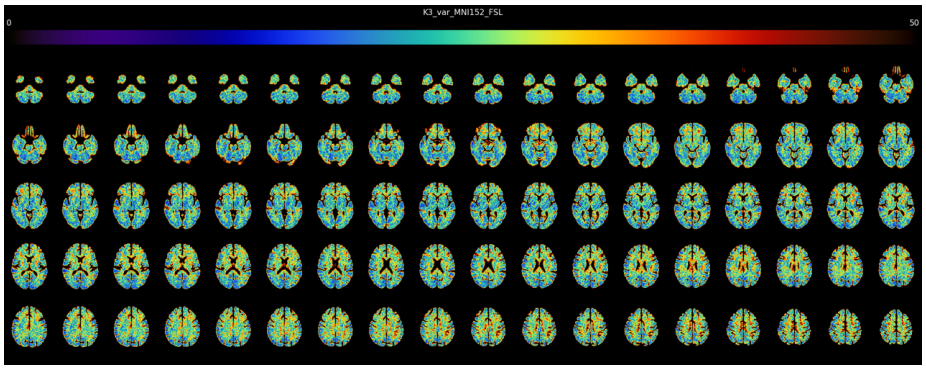

(b) k_3 CV%

Figure 3.13: k_3 average map and CV%

Multislice axial visualization of k_3 average across subjects and corresponding CV

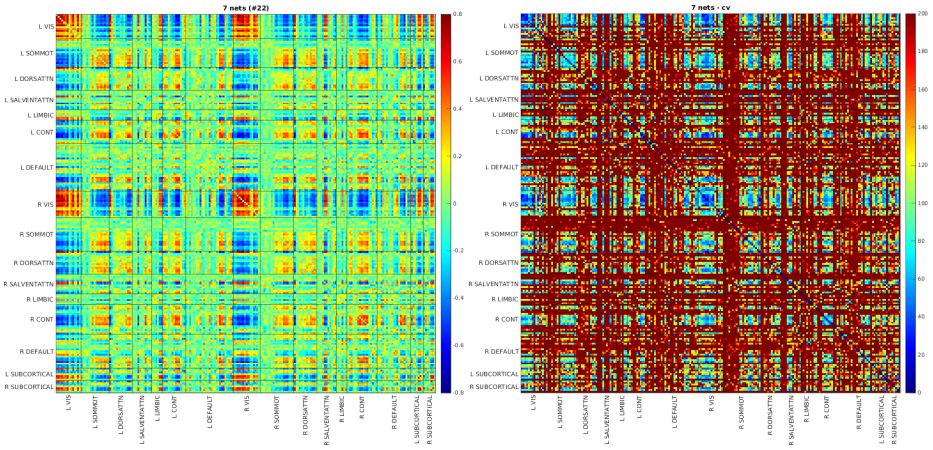

(a) Mean matrix (b) CV

Figure 3.14: Metabolic Connectivity

Metabolic Connectivity: average matrix (a) and CV (b), obtained applying Pearson's correlation on parcels time-seres (Schaefer 7 nets cortical atlas and 14 FIRST subcortical)

centile) in order to highlight the highest correlation values, and are represented in figure 3.15. For K_1, a clear modular structure does not seem to emerge for functional networks, whereas for k_3 within-network correlation survive thresholding for VIS and part of the SMN.

3.1.4 FC and features computation

Time-series

FC average matrix is represented in figures 3.16. From visual inspection, two modules can be easily identified: one comprising VIS, SMN, DAN and VAN (both ipsilateral and controlateral), and the other distributed across parcels of the DMN and the FPN.

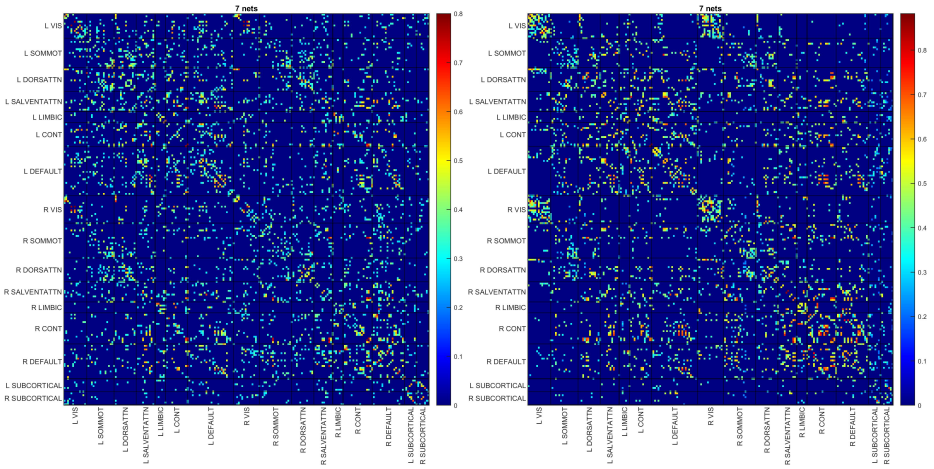

(a) K_1 (b) k_3

Figure 3.15: K_1 and k_3 across-subjects connectivity

K_1 (a) and k_3 (b) across subjects connectivity matrices were sparsified (90^{th} percentile) in order to highlight the most meaningful correlations

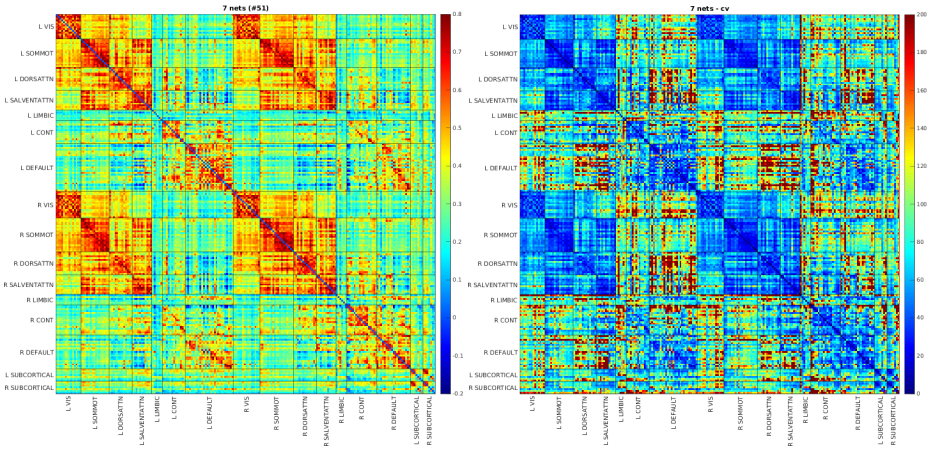

(a) Mean matrix (b) CV

Figure 3.16: Functional Connectivity

Functional Connectivity: average matrix (a) and CV (b), obtained applying Pearson's correlation on parcels time-seres (Schaefer 7 nets cortical atlas and 14 FIRST subcortical)

Subject-series

Across subjects correlation matrices for fMRI features GFC and ReHo, parcelled using the Schaefer cortical and FIRST subcortical atlas (214 regions), were made sparse (90^{th} percentile) in order to highlight the highest correlation values, and are represented in figures 3.17.
For GFC, parcels within VIS and DMN shows high correlation, which survives sparsification. Correlation is also strong between some parcels belonging to DMN and FPN.
For ReHo, similar modularity emerges: VIS and DMN within-networks connections are preserved, and the same can be said about FPN and DMN between-networks connections. Differently from GFC, the connections within SMN are maintained, particularly on the right hemisphere.

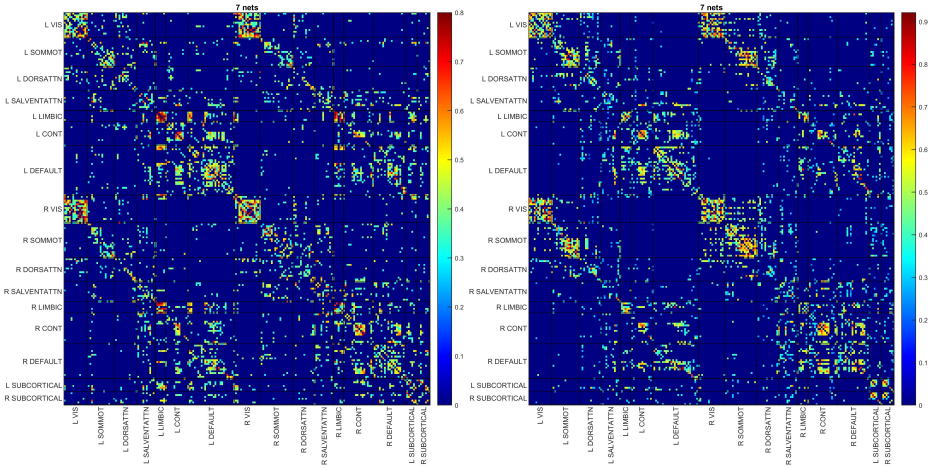

(a) GFC (b) ReHo

Figure 3.17: GFC and ReHo across-subjects connectivity

GFC (a) and ReHo (b) across subjects matrices were sparsified (90^{th} percentile) in order to highlight the most meaningful correlations

3.2 Connectivity Gradients and PET-fMRI multimodal integration

3.2.1 Time-series analysis

Components obtained from LE application are sorted decreasingly according to their relative importance, providing metabolic and functional *gradients*.

Gradients Maps obtained from MC average matrix are shown in figures 3.18 and 3.19. Gradients derived from both sparsified and unsparsified matrix have

a similar cortical distribution. First gradient separates the occipital lobe, part of the temporal lobe and part of the cingulate gyrus from the frontal and parietal lobes, whereas second gradient groups together occipital lobe and lateral prefrontal cortex at one end of the scores distribution, whereas medial prefrontal cortex, cingulate gyrus and temporal lobes are at the opposite end.
In figure 3.20, G1 scores are plotted against G2 scores: VIS parcels are markedly separated from the other networks.

(a) G1 (b) G2

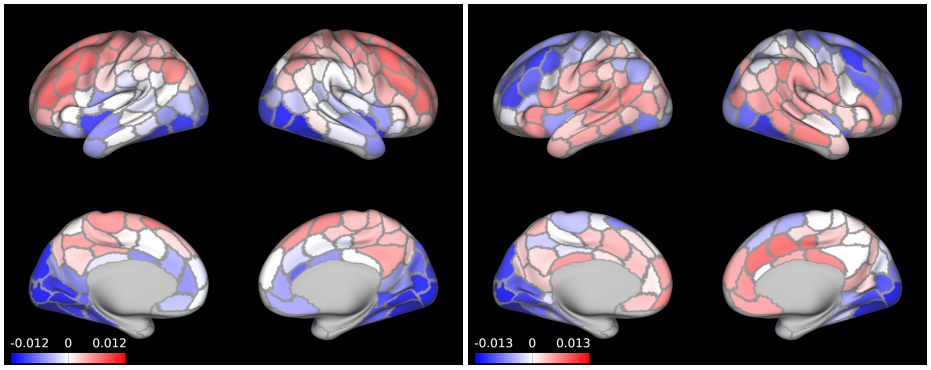

(c) Eigenvalues

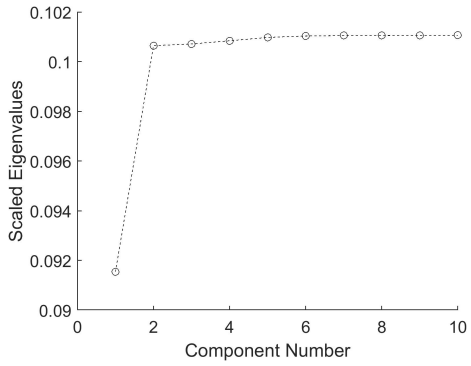

Figure 3.18: Unsparsified MC gradients

(a) G1 separates the occipital lobe, part of the temporal lobe and part of the cingulate gyrus from the frontal and parietal lobes.
(b) G2 groups together occipital lobe and lateral prefrontal cortex at one end of the scores distribution, whereas medial prefrontal cortex, cingulate gyrus and temporal lobes are at the opposite end

Gradients Maps obtained from unsparsified FC average matrix are represented in figure 3.21. G1 divides DMN from VIS and SMN, whereas G2 sepa-

(a) G1

(b) G2

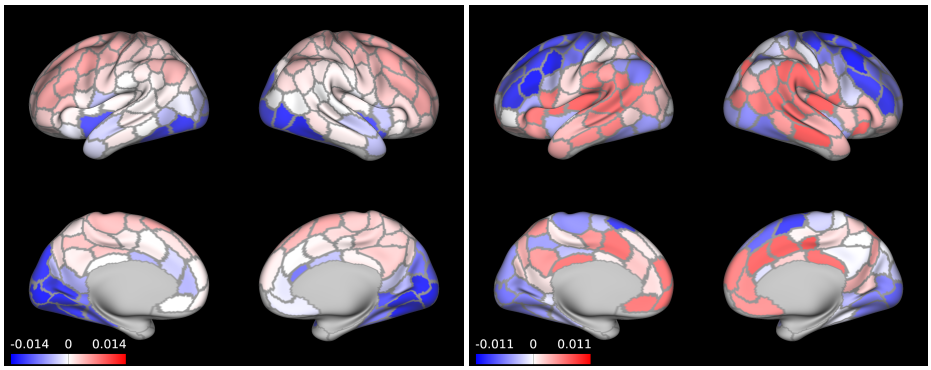

(c) Eigenvalues

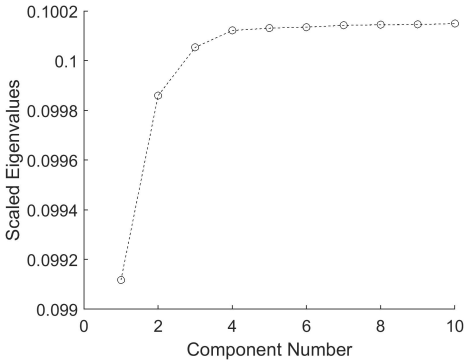

Figure 3.19: Sparsified MC gradients

Cortical gradient scores distribution is similar to the unsparsified version, with some minor differences in ventromedial prefrontal cortex

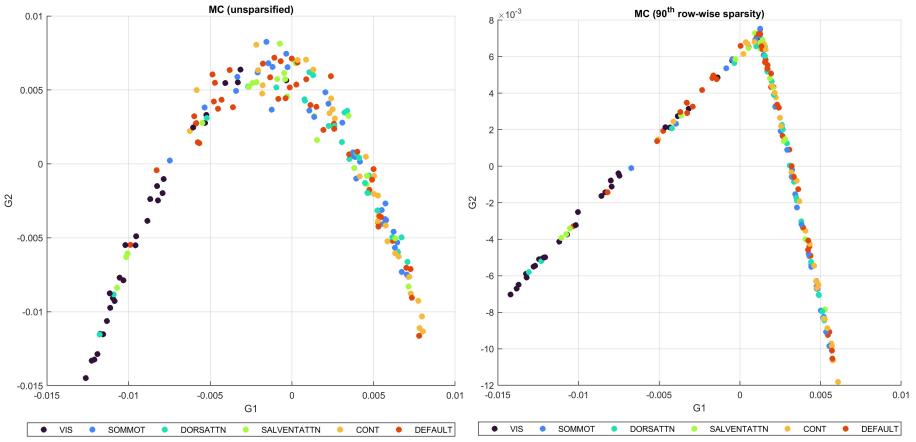

(a) (b)

Figure 3.20: MC: gradients scatter plot

Scatter plot of MC G1 scores and G2 scores, from unsparsified (a) and sparsified (b) input matrix. VIS parcels are almost completely separated from the others and concentrated towards G1 negative values

rates occipital and lateral prefrontal areas from medial prefrontal cortex, parietal and temporal lobes. Sparsified matrix gives sligthly different results, with G1 dividing VIS from SMN, and G2 having DMN and VIS at the opposite ends of scores distribution. This networks separation can also be observed in figure 3.23, where first two gradients scores are plotted on the same plane.

Gradients derived from joint alignment are represented in figure 3.24. First order gradients provide a similar cortical organization for both MC and FC, dividing occipital region from the rest of the brain. Second order gradient shows different architecture for the two modalities: in MC occipital lobe is separated from prefrontal cortex, whereas in FC, second gradient divides DMN from SMN.

Comparing the first and second order MC and FC gradients using Pearson's coefficient, significant correlations were found between FC G1 and MC G1, FC G2 and MC G1, FC G2 and MC G2 (see figure 3.25). Maixmum overlapping areas for first gradients of MC and FC are located over VIS and SMN. Overlapping regions between FC G1 and second MC G2 belong to VAN and SMN. Matching areas between second FC gradient and first MC gradient comprise VIS and DMN areas (mostly prefrontal cortex and precuneus). Second FC and MC gradients share areas located over the medial prefrontal cortex, the precuneus and the temporal lobe, mostly belonging to DMN.

(a) G1

(b) G2

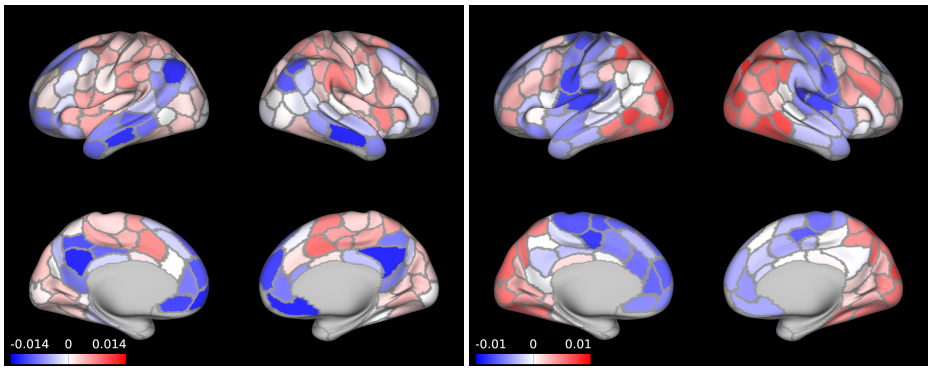

(c) Eigenvalues

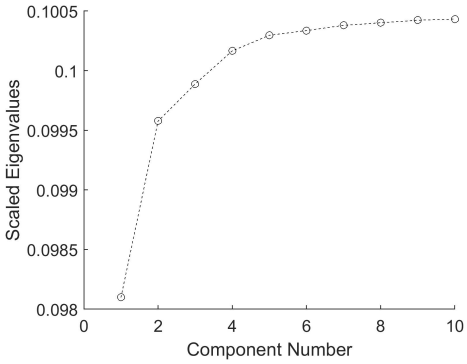

Figure 3.21: Unsparsified FC gradients

(a) G1 divides DMN from VIS and SMN. (b) G2 separates occipital and lateral prefrontal areas from medial prefrontal cortex, parietal and temporal lobes.

(a) G1

(b) G2

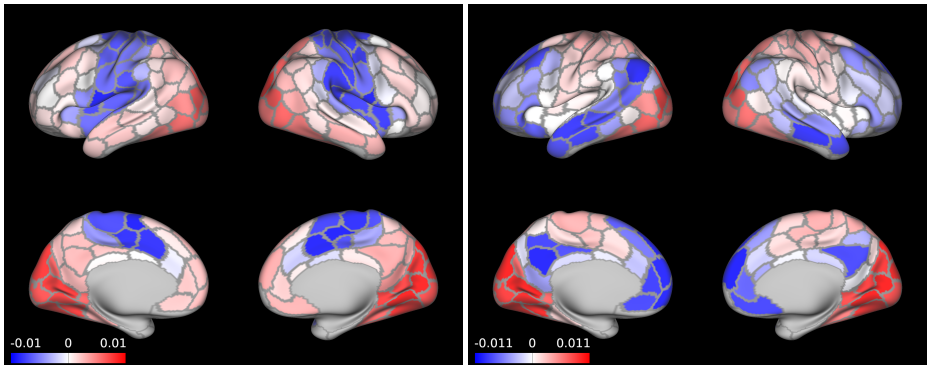

(c) Eigenvalues

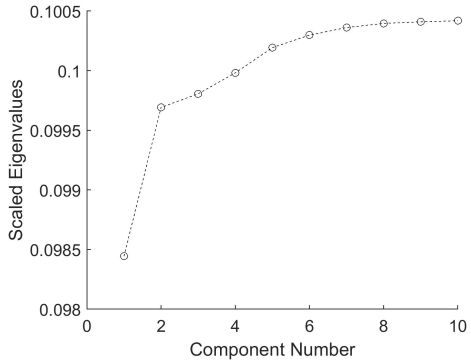

Figure 3.22: Sparsified FC gradients

(a) G1 divides VIS from SMN. (b) G2 has negative values on DMN and positive values on VIS

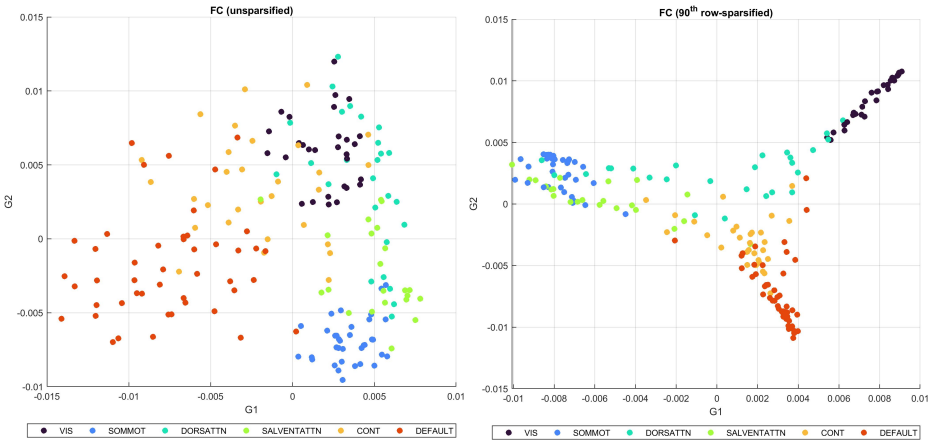

(a) (b)

Figure 3.23: FC: gradients scatter plot

First two FC gradients scores, from unsparsified (a) and sparsified (b) input matrix, are plotted together. In here, typical transmodal-unimodal gradient seems to be delineated, with DMN separated from SMN and VIS

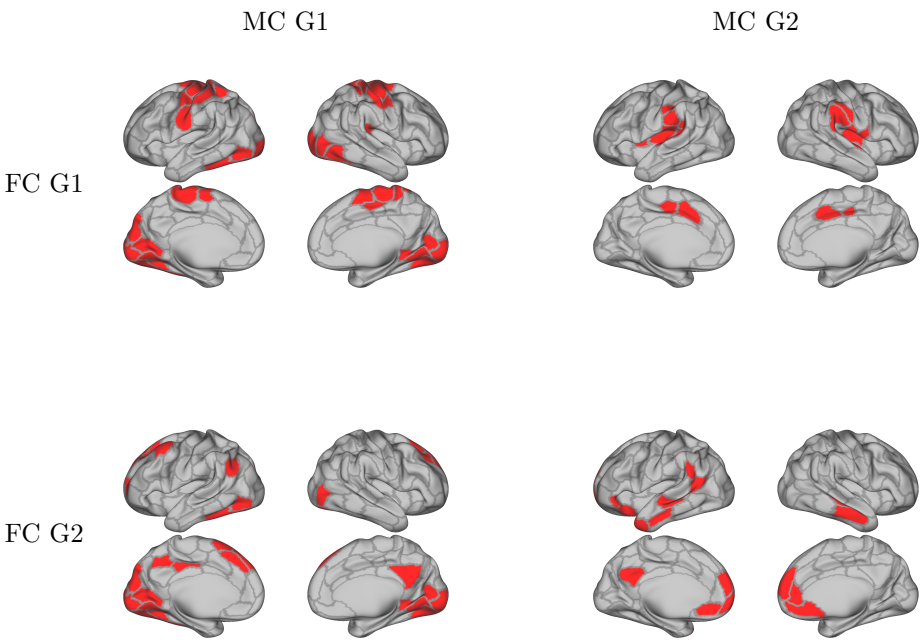

Figure 3.26: Overlapping regions of metabolic and functional gradients

Maixmum overlapping areas for first gradients of MC and FC are located over VIS and SMN. Overlapping regions between FC G1 and second MC G2 belong to VAN and SMN. Matching areas between second FC gradient and first MC gradient comprise VIS and DMN areas (mostly prefrontal cortex and precuneus). Second FC and MC gradients share areas of the medial prefrontal cortex, precuneus and parcels over the temporal lobe, all belonging to DMN.

(a) MC G1

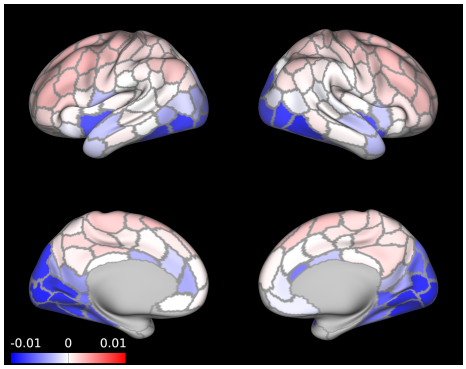

(b) MC G2

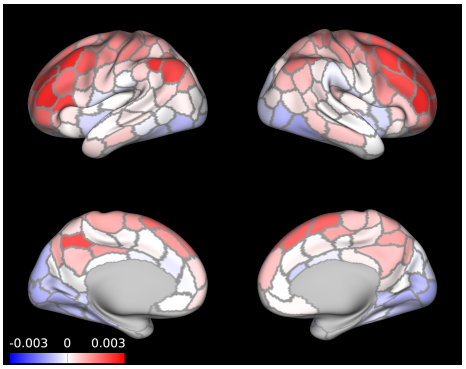

(c) FC G1

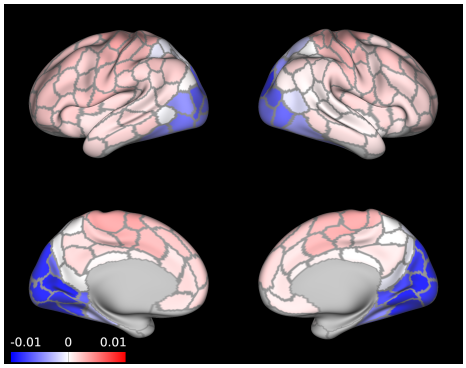

(d) FC G2

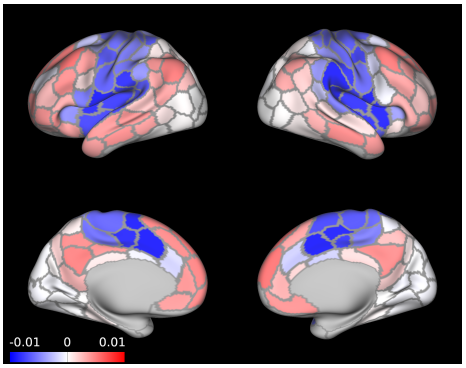

(e) Eigenvalues

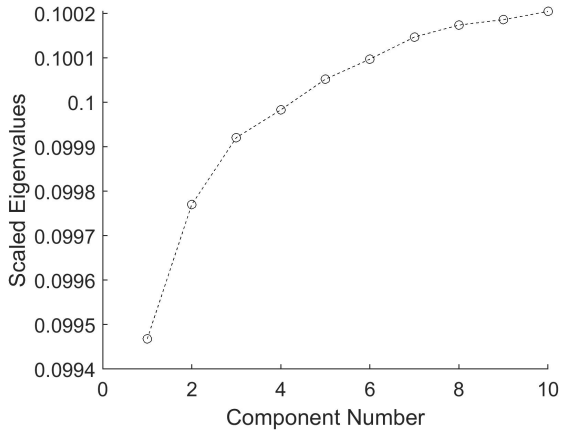

Figure 3.24: Joint Alignment of MC and FC gradients

In here, both matrices were embedded together in the new space. Similar spatial pattern is shared by first order gradients scores of the two modalities, whereas second FC gradient seems to maintain unimodal-transmodal architecture

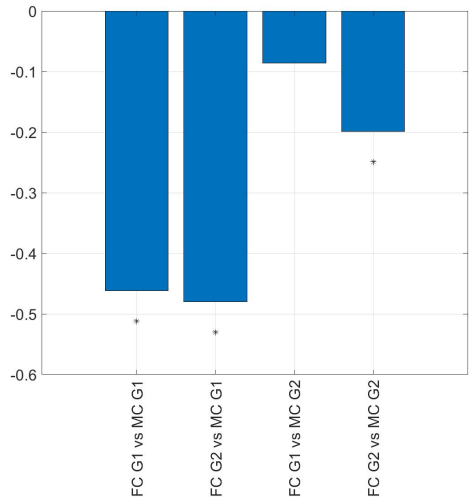

Figure 3.25: Pearson's correlation between first and second order MC and FC gradients

FC G1 and MC G1 are significantly anticorrelated, and so are FC G2 and MC G1, which exhibit the strongest correlation. Anticorrelation between FC G2 and MC G2 is moderate but significant

3.2.2 Subject-series analysis

For K1, G1 divides areas of the cingulate gyrus, precuneus and somatomotor cortex from parcels belonging to occipital and prefrontal cortex, whereas G2 groups together areas of occipital and ventromedial prefrontal cortex on one side, and parcels from the dorsal prefrontal cortex on the other (figure 3.27). Plotting K_1 G1 and G2 scores on the same plane (figure 3.29a), no clear division can be noticed for functional networks.
For k_3, areas of the cingulate gyrus and precuneus have the highest G1 scores whereas parcels of the prefrontal cortex have the lowest. No symmetric pattern emerges from G2 scores distribution between the two hemispheres, apart from the occipital lobe (figure 3.28). Observing scatter plot of first two k_3 gradients scores, VIS seems well separated from the other networks (figure 3.29b).

For GFC, G1 separates VIS and SMN from prefrontal cortex, cingulate gyrus, precuneus and temporal lobe, while G2 groups together VIS, medial prefrontal cortex, and temporal lobe at one end of scores distribution, and dorsolateral prefrontal cortex at the opposite (figure 3.30).
ReHo first gradient separates VIS and SMN from regions corresponding to ventral prefrontal cortex and part of the cingulate gyrus. G2 separates occipital and temporal areas from dorsomedial and ventromedial prefrontal cortex (figure 3.31).

Comparing the first and second order K_1 and GFC gradients using Pearson's coefficient, significant correlations were found between GFC G1 and K_1

(a) G1

(b) G2

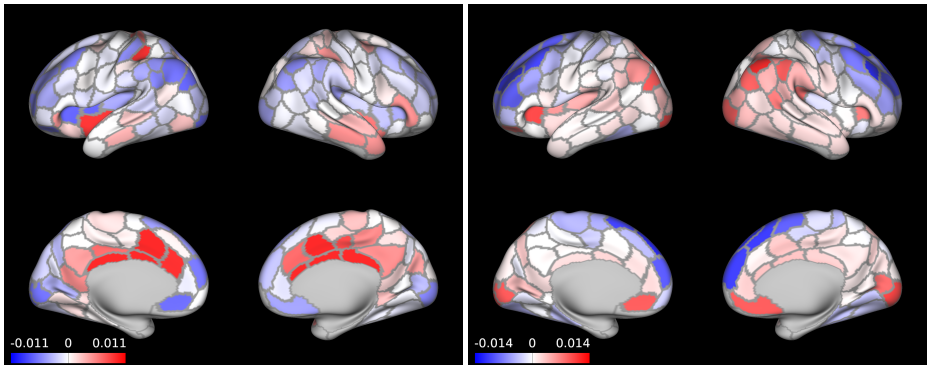

(c) Eigenvalues

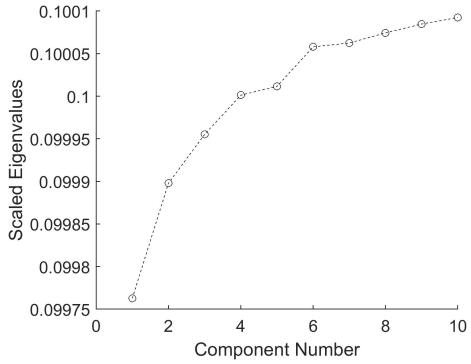

Figure 3.27: K_1 gradients

(a) G1 divides areas of the cingulate gyrus, precuneus, somatomotor cortex from parcels belonging to occipital and prefrontal cortex.
(b) G2 has positive values on ventromedial prefrontal cortex and occipital lobe, and negative values on dorsal prefrontal cortex

(a) G1

(b) G2

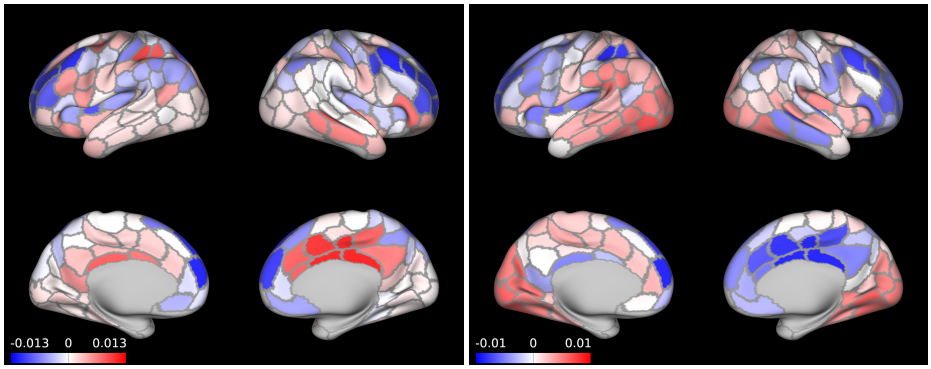

(c) Eigenvalues

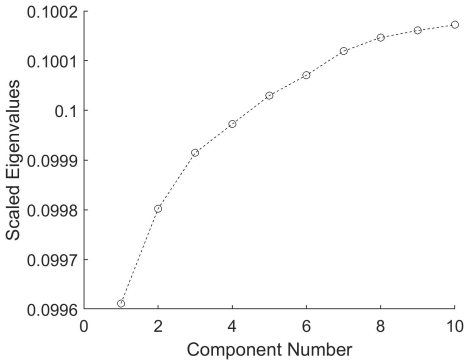

Figure 3.28: k_3 gradients

(a) G1 has areas of the cingulate gyrus and precuneus on the negative side of the scores distribution, and some parcels of the prefrontal cortex on the opposite.
(b) No symmetric pattern emerges from G2 between the two hemispheres, apart from the occipital lobe, whose parcels have the same polarity

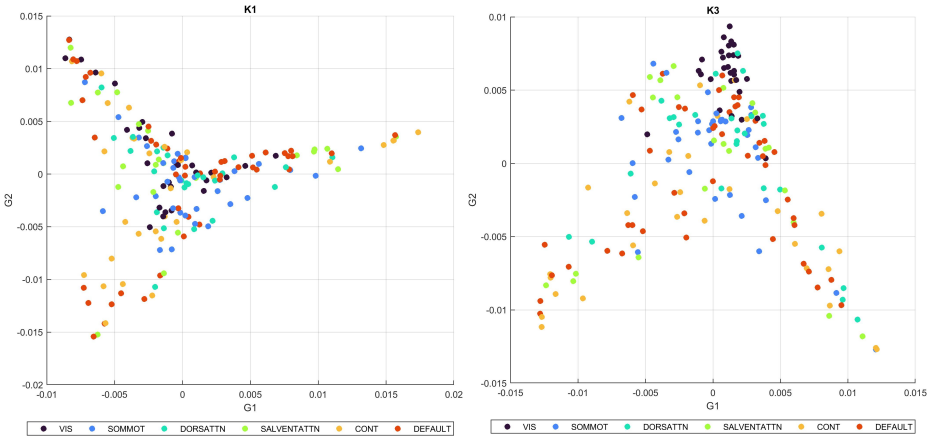

(a) K_1 (b) k_3

Figure 3.29: Gradients Scatter plot for K_1 and k_3

Scatter plot of K_1 (a) and k_3 (b) G1 and G2 scores. No clear networks separation emerges, apart from VIS in k_3

G1, GFC G2 and K_1 G1, GFC G2 and K_1 G2 (see figure 3.33a). Maixmum overlapping areas for first gradients of K_1 and GFC are located over cingulate gyrus and part of the occipital lobe. Overlapping regions between GFC G1 and K_1 G2 are just a few parcels on the prefrontal cortex and occipital lobe. Matching areas between GFC G2 and K_1 G1 are moslty located over the lateral prefronal cortex and cingulate gyrus area. GFC G2 and K_1 G2 matches on ventromedial prefrontal cortex, dorsolateral prefrontal cortex and occipital lobe (see figure 3.34).
Comparing the first and second order K_1 and ReHo gradients using Pearson's coefficient, significant correlations were found between ReHo G2 and K_1 G1, ReHo G2 and K_1 G2 (see figure 3.33b). Best overlapping areas are mostly located over the prefrontal cortex and cingulate gyrus (see figure 3.35).

Comparing the first and second order k_3 and GFC gradients using Pearson's coefficient, significant positive correlations were found between GFC G2 and k_3 G1, GFC G2 and k_3 G2, whereas significant negative correlation was found between GFC G1 and k_3 G2 (see figure 3.36a). Maixmum overlapping areas for first gradients of k_3 and GFC are located mostly over cingulate gyrus. Overlapping regions between GFC G1 and k_3 G2 belong to occipital lobe, cingulate gyrus. Matching areas between GFC G2 and k_3 G1 are located over the lateral prefronal cortex and cingulate gyrus area. GFC G2 and k_3 G2 matches almost entirely on the occipital lobe (see figure 3.37).
Comparing the first and second order k_3 and ReHo gradients using Pearson's coefficient, significant positive correlations were found between ReHo G2 and k_3 G1, ReHo G2 and k_3 G2, whereas significant negative correlation was found betweem ReHo G1 and k_3 G2 (see figure 3.36a). ReHo G1 and k_3 G1 matches in

(a) G1

(b) G2

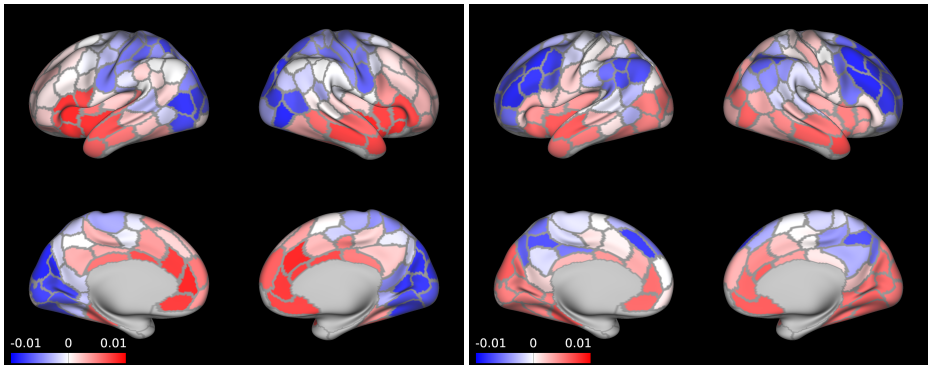

(c) Eigenvalues

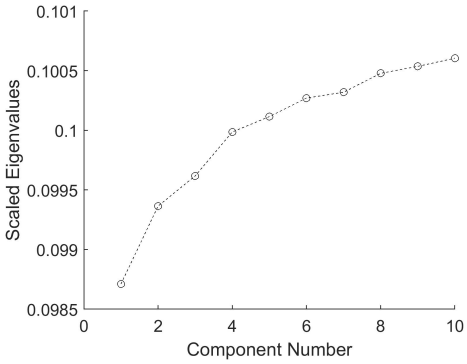

Figure 3.30: GFC gradients

(a) G1 separates VIS and SMN from prefrontal cortex, cingulate gyrus, precuneus and temporal lobe.
(b) G2 groups together VIS, medial prefrontal cortex, and temporal lobe on one side of scores distribution, whereas dorsolateral prefrontal cortex is on the opposite side

(a) G1

(b) G2

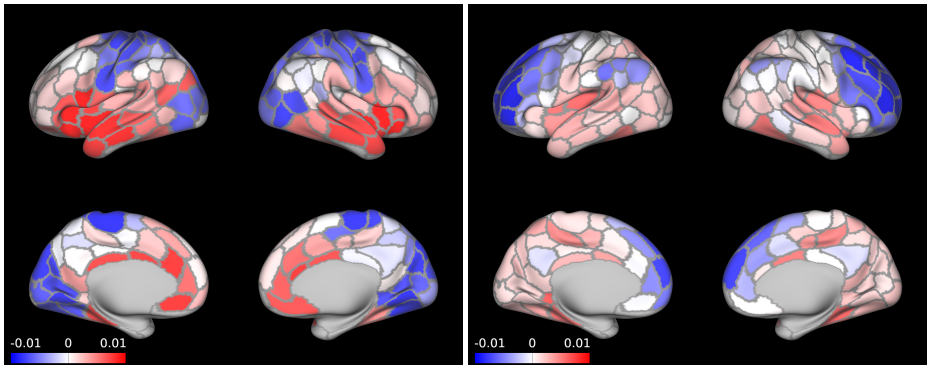

(c) Eigenvalues

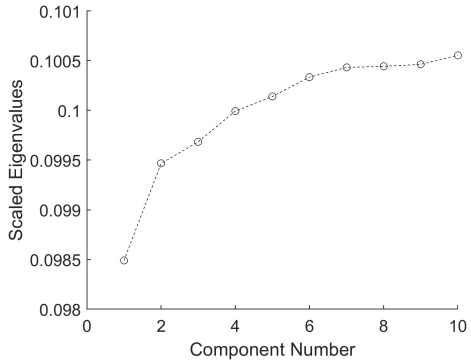

Figure 3.31: ReHo gradients

(a) G1 has negative values on VIS and SMN and positive values on ventral prefrontal cortex and part of the cingulate gyrus.
(b) G2 separates occipital and temporal areas from dorsomedial and ventromedial prefrontal cortex

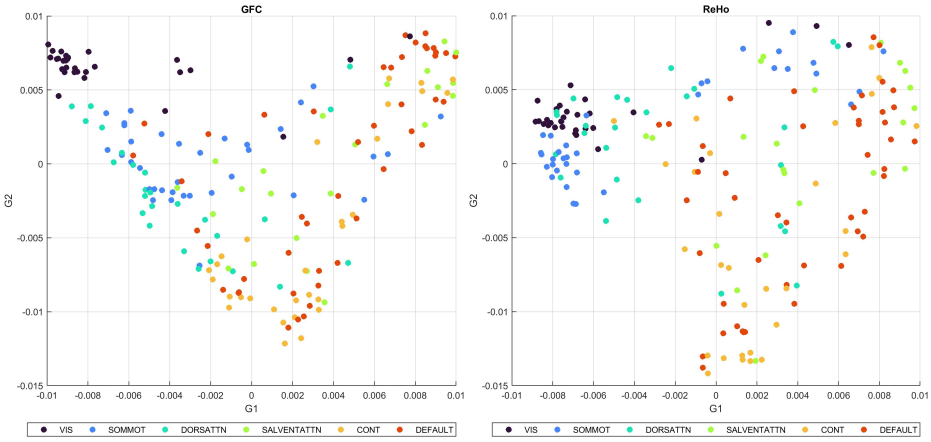

(a) GFC (b) ReHo

Figure 3.32: Gradients Scatter plot for GFC and ReHo

For both parameters VIS parcels are collocated on a specific area identified by the two gradients

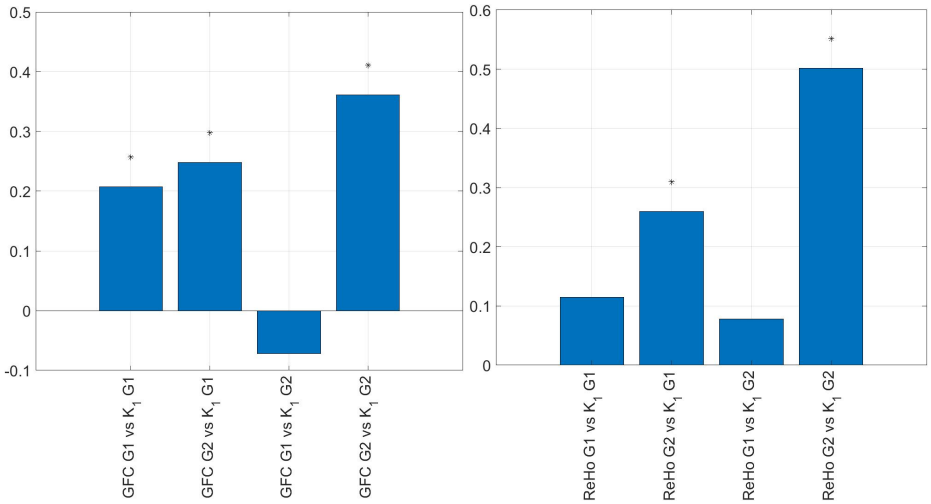

(a) GFC vs K_1 (b) ReHo vs K_1

Figure 3.33: Pearson's correlation between first and second order gradients of K_1 with GFC and ReHo

(a) GFC G1 significantly correlates with K_1 G1, whereas GFC G2 significantly correlates with first and second K_1 gradients.
(b) As for ReHo, G2 significantly correlates with both K_1 gradients

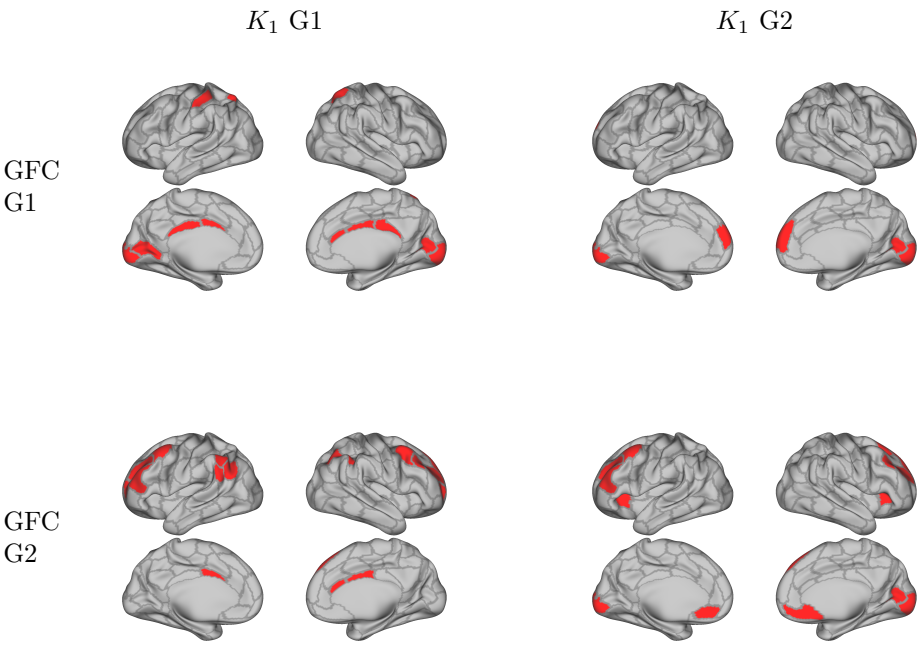

Figure 3.34: Overlapping regions for K_1 and GFC gradients

Parcels in red are the ones where most extreme values of gradients distribution overlaps for the two parameters. Cingulate area and a few parcels on the occipital lobes overlap recurrently

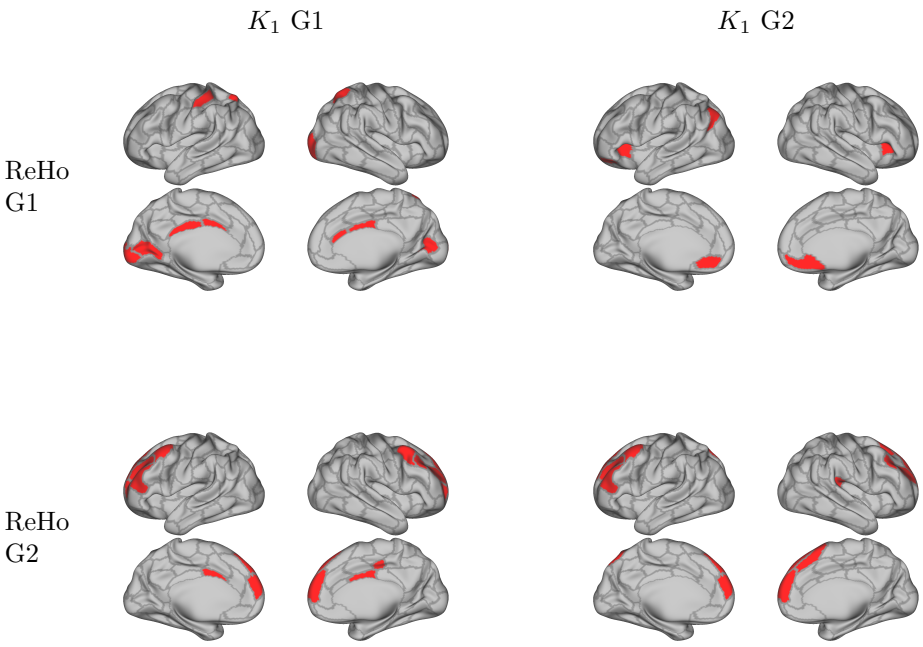

Figure 3.35: Overlapping regions for K_1 and ReHo gradients

Parcels in red are the ones where most extreme values of gradients distribution overlaps for the two parameters. Cingulate area and dorsomedial prefronatl cortex overlap recurrently

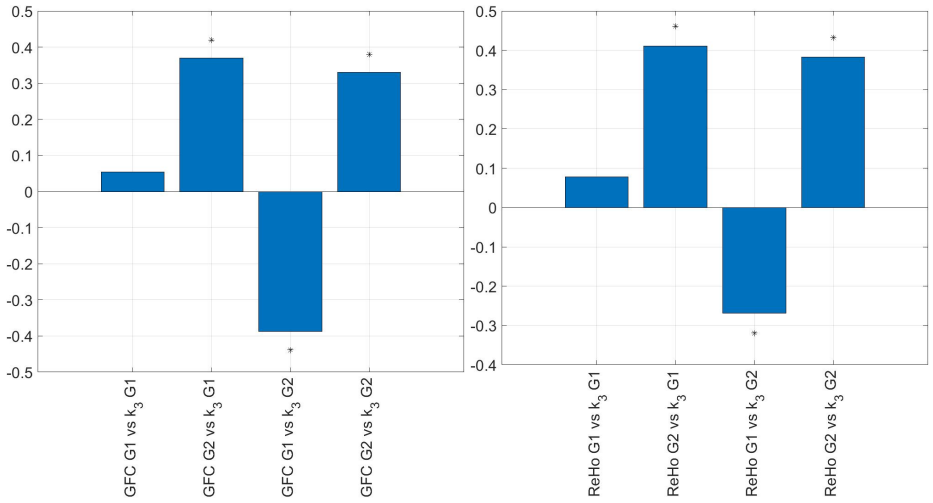

(a) GFC vs k_3 (b) ReHo vs k_3

Figure 3.36: Pearson's correlation between first and second order gradients of k_3 with GFC and ReHo

(a) GFC G2 is significantly correlated with k_3 G1 and G2, whereas GFC G1 is significantly anticorrelated with k_3.
(b) ReHo G2 is significantly correlated with k_3 G1 and G2, whereas ReHo G1 is significantly anticorrelated with k_3.

the cingulate gyrus. ReHo G2 and k_3 G2 overlaps on the occipital lobe. ReHo G2 and k_3 G1 share some parcels in the prefrontal cortex and cingulate gyrus. Finally ReHo G2 and k_3 G2 share some parcels distributed over the prefrontal cortex 3.38).

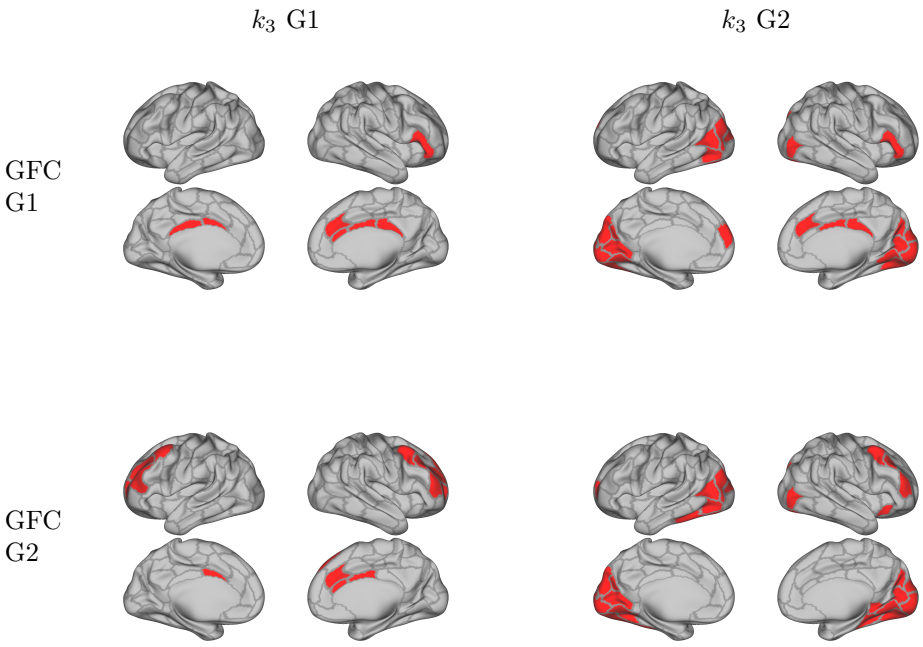

Figure 3.37: Overlapping regions for k_3 and GFC gradients

GFC and $k3$ gradients recurrently overlap on cingulate gyrus and occipital lobe

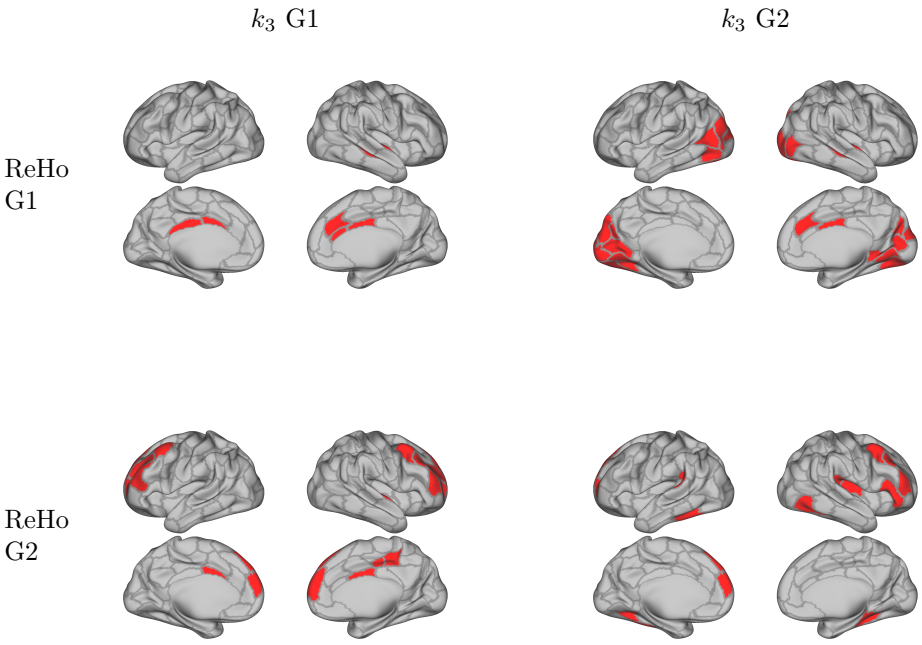

Figure 3.38: Overlapping regions for k_3 and ReHo gradients

ReHo and $k3$ gradients recurrently overlap on cingulate gyrus, occipital lobe and prefrontal cortex

Chapter 4

Discussion

4.1 IDIF-based [^{18}F]FDG quantification

In this thesis project, quantification of [^{18}F]FDG microparameters has been performed using an IDIF. As already discussed, this is a non invasive alternative to arterial blood sampling, which could help translation of dynamic PET to clinical practice. If, on the one end, it is true that the approach employed for IDIF derivation is not entirely blood-free, as it relies on collection of venous blood from the patient to perform Chen's correction, venous sampling is still less dangerous than arterial cannulation, and the number of samples required can be limited to just three, undoubtedly causing less discomfort to the patient. We have actually shown that a completely blood-free approach can still be achieved using model-based estimates (as with nonlinear mixed effect modeling) of plasma radioactivity concentration from other physiological covariates [58]. One of the problem usually connected with IDIF estimation is represented by radio-metabolites correction: however, this is not addressed in this thesis since [^{18}F]FDG doesn't produce radio-metabolites.
The extraction site for the approximated $C_p(t)$ has been identified as the internal carotid arteries, which is a well-documented option for ECAT HR+ scanners, when taking their limited FOV in consideration. Since these structures are affected by spillover due to their small caliber, we adopted Chen's model to correct the extracted curve [11]. The same model was evaluated and compared to the existing alternatives for IDIF derivation in [64]: in the cited study, using phantom data the estimated curve correlated with the reference curve, whereas using clinical data the peak was systematically underestimated. This could be critical, as one of the main problems which hindered the use of IDIF for microparameter estimates is their sensitivity to the the shape of the curve, and especially to the early part. However, in [64] the authors hypothesizes that the peak underestimation may be due to the inadequate sampling grid of the employed clinical studies, whose first 12 time frames last 10 seconds. In our data, sampling grid is denser in the beginning (25 frames of 5 seconds), and so we

suppose that artifacts coming from limited temporal resolution should be limited. As for the resulting shape of the IDIF, we also noticed that the rescaling of the curve by the estimaed RC from Chen's model contribute to increase peak amplitude, therefore compensating for spill-out effects affecting peak. However, comparison with the gold standard AIF would be useful to evaluate the extracted IDIF and to efficiently address potential problems
One of the main advantage of our IDIF extraction algorithm is that it depends on a semi-automatic procedure, which only requires manual intervention in tuning parameters useful for slices selection and vesselness probability map binarization. As a result, no manual segmentation of the carotids arteries was needed, which would be a time-consuming and potentially error-prone procedure. Moreover, vascular segmentation didn't rely on coregistration to structural or angiographic images and was only based on the use of PET scans. An important component of this algorithm is represented by arterial voxels selection[40]: this ensures that only the best TACs are averaged to obtain the IDIF curve, without introducing bias coming from non arterial voxels activity which are comprised in the automatically segmented vascular ROI. A possible extension to the analysis performed on this dataset could be represented by the comparison of the arterial and venous IDIF, as shown in [45]. In particular, Superior Sagittal Sinus(SSS) can be easily segmented, as it is done here for arterial peak estimation. Having bigger caliber, SSS should be less affected by activity from sorrounding tissues. However, venous peak is slower than arterial peak, as it is physiologically plausible and also confirmed by the analysis carried out for automatic carotid segmentation in our images. Model based correction to estimate arterial IDIF from venous IDIF may still be employed to make good use of veins segmentation. With the same rationale, it would be possible to evaluate the effect of Chen's correction using SSS IDIF rather than the blood samples, so as to have a completely blood-free IDIF extraction algorithm. For large axial FOV scanners (e.g., PET/MR, newer PET/CTs like Siemens Biograph Vision), another candidate site for IDIF extraction is represented by common carotid arteries (CCA), which have bigger caliber than ICAs and whose sorrounding tissues generally show low [^{18}F]FDG uptake [45].
Microparameters estimation using VB approach yielded good results at voxel-level, showing consistent parameters estimates across subjects. Validation using gold standard approach for AIF extraction would be useful to fully evaluate the effect of IDIF on rate constants estimates.

4.2 [^{18}F]FDG and rsfMRI multimodal integration

Gradients derivation for time-series FC average confirmed what was previously presented in literature [31]. First two gradients shows a clear network separation for DMN, SMN and VIS, probably reflecting the synaptic hierarchy postulated by Mesulam [33]. FPN, despite being separated from the remaining networks,

end up being close to DMN parcels, especially using a sparsified input matrix, probably by reason of its transmodal nature. Interpreting VAN and DAN collocation in the plane identified by the first two gradients is not straightforward. Interestingly, some VAN parcels are distributed among SMN parcels, and the two attention networks do not overlap in this representation. This may be intended as proof of their distinctive roles in cognition.
As for time-series MC average networks, first two gradients allow identification of just the VIS. First order metabolic and functional gradients exhibit significant correlation, but seem to overlap mostly in unimodal regions rather than in transmodal ones. The same is not true for the other combination between first and second order gradients, which overlap in parcels belonging to DMN, even if the match never include the whole network.

From these results, it could be hypothesized that metabolic networks have a specific cortical organization. However, it should be noted that there's still no gold standard for time-series MC calculation, and results seem to largely depend on multicollinearities and to the kind of normalization applied [59]. Since gradients proved to be a useful methodology for integration of information coming from different modalities (as for structural and functional imaging in [36]), such an experiment could be repeated once a new robust approach for MC matrix derivation has been reached.
In this thesis it was also presented a first attempt of gradients application to across-subject connectivity matrix. From a metabolic perspective, it is known how K_1 and k_3 have different physiological interpretation, with K_1 representing [^{18}F]FDG influx rate from plasma to tissue, and k_3 representing tracer phosphorylation by hexokinase enzyme. This is reflected also in gradient maps, which show a different spatial organization for the two parameters. Similarly to what happens with time-series MC, VIS emerges as a distinct network in the first two gradients space for k_3. As regards fMRI features, similar spatial pattern can be observed for GFC and ReHo first order gradients, showing that the two metrics share some spatial properties, whereas some dissimilarity seem to emerge from second order gradient distribution. Comparison between the functional and metabolic parameters may surely contribute to characterize how much global and local synchronization affect metabolism. The fact that significant correlation was found between gradients from all combination of functional and metabolic parameters may be interpreted as proof of the metabolic burden associated to brain functional connections, as already revealed in terms of the increase in metabolism associated with the degree of connectivity[51].

Chapter 5

Conclusions and future perspectives

The [^{18}F]FDG data analysis led to the development of a semi-automatic pipeline for IDIF derivation, starting from vessels segmentation up to AIF model fitting and spillover correction. This could be easily adapted to other studies and the district of choice for $C_p(t)$ extraction could be easily modified according to specific needs. For this thesis project, IDIF was successfully extacted from internal carotid arteries and, combined with Variational Bayesian approach, led to reliable voxel-wise microparameters estimates. However, validation using arterial $C_p(t)$ would be useful to assess the sensitivity of microparameters estimates to the use of the IDIF rather than the AIF, which is the gold standard.

Gradients were used for the first time as an integration method of metabolic and functional connectivity measures at group level. MC gradients may depend on the normalization approach employed for managing TACs multicollinarities, and since there's still no gold standard for time-series MC derivation, results are to be intended as preliminary. However, comparison through gradients may still be a valuable option for studying metabolic demand of resting-state activations. Effects of using different kernel functions or different dimensionality reduction techniques for MC gradients need to be explored. In particular, using a linear technique, such as PCA, or other nonlinear techniques, as DM, may represent a possible future extension to the analysis performed so far. Such a modality could be also extended to the derivation of subject level functional and metabolic connectivity gradients, which could prove useful for investigating metabolism in phyisiological or pathological conditions.

Bibliography

[1] Mario Amend, Tudor M. Ionescu, Xin Di, Bernd J. Pichler, Bharat B. Biswal, and Hans F. Wehrl. Functional resting-state brain connectivity is accompanied by dynamic correlations of application-dependent [18F]FDG PET-tracer fluctuations. *NeuroImage*, 196:161–172, 8 2019.

[2] Alan Anticevic, Sien Hu, Sheng Zhang, Aleksandar Savic, Eileen Billingslea, Suzanne Wasylink, Grega Repovs, Michael W. Cole, Sarah Bednarski, John H. Krystal, Michael H. Bloch, Chiang-Shan R. Li, and Christopher Pittenger. Global resting-state functional magnetic resonance imaging analysis identifies frontal cortex, striatal, and cerebellar dysconnectivity in obsessive-compulsive disorder. *Biological Psychiatry*, 75:595–605, 4 2014.

[3] Claude J. Bajada, Lucas Q. Costa Campos, Svenja Caspers, Richard Muscat, Geoff J.M. Parker, Matthew A. Lambon Ralph, Lauren L. Cloutman, and Nelson J. Trujillo-Barreto. A tutorial and tool for exploring feature similarity gradients with MRI data. *NeuroImage*, 221, 11 2020.

[4] Giulia Baracchini, Bratislav Mišić, Roni Setton, Laetitia Mwilambwe-Tshilobo, Manesh Girn, Jason S. Nomi, Lucina Q. Uddin, Gary R. Turner, and R. Nathan Spreng. Inter-regional BOLD signal variability is an organizational feature of functional brain networks. *NeuroImage*, 237:118149, 8 2021.

[5] Michaël Bernier, Etienne Croteau, Christian Alexandre Castellano, Stephen C. Cunnane, and Kevin Whittingstall. Spatial distribution of resting-state BOLD regional homogeneity as a predictor of brain glucose uptake: A study in healthy aging. *NeuroImage*, 150:14–22, 4 2017.

[6] A. Bertoldo, P. Vicini, G. Sambuceti, A.A. Lammertsma, O. Parodi, and C. Cobelli. Evaluation of compartmental and spectral analysis models of [18F]FDG kinetics for heart and brain studies with PET. *IEEE Transactions on Biomedical Engineering*, 45:1429–1448, 1998.

[7] Alessandra Bertoldo, Gaia Rizzo, and Mattia Veronese. Deriving physiological information from PET images: From SUV to compartmental modelling, 2014.

[8] Bharat Biswal, F. Zerrin Yetkin, Victor M. Haughton, and James S. Hyde. Functional connectivity in the motor cortex of resting human brain using echo-planar MRI. *Magnetic Resonance in Medicine*, 34:537–541, 10 1995.

[9] Ewart Carson and Claudio Cobelli. Modelling methodology for physiology and medicine second edition, 2014.

[10] M. Castellaro, G. Rizzo, M. Tonietto, M. Veronese, F.E. Turkheimer, M.A. Chappell, and A. Bertoldo. A Variational Bayesian inference method for parametric imaging of pet data. *NeuroImage*, 150:136–149, 4 2017.

[11] Kewei Chen, Daniel Bandy, Eric Reiman, Sung-Cheng Huang, Michael Lawson, Dagan Feng, Lang-Sheng Yun, and Anita Pal. Noninvasive Quantification of the Cerebral Metabolic Rate for Glucose Using Positron Emission Tomography, 18 F-Fluoro-2-Deoxyglucose, the Patlak Method, and an Image-Derived Input Function, 1998.

[12] Maurizio Corbetta and Gordon L. Shulman. Control of goal-directed and stimulus-driven attention in the brain. *Nature Reviews Neuroscience*, 3:201–215, 3 2002.

[13] Timothy L. Davis, Kenneth K. Kwong, Robert M. Weisskoff, and Bruce R. Rosen. Calibrated functional MRI: Mapping the dynamics of oxidative metabolism. *Proceedings of the National Academy of Sciences*, 95:1834–1839, 2 1998.

[14] Reinder Vos de Wael, Oualid Benkarim, Casey Paquola, Sara Lariviere, Jessica Royer, Shahin Tavakol, Ting Xu, Seok Jun Hong, Georg Langs, Sofie Valk, Bratislav Misic, Michael Milham, Daniel Margulies, Jonathan Smallwood, and Boris C. Bernhardt. Brainspace: a toolbox for the analysis of macroscale gradients in neuroimaging and connectomics datasets. *Communications Biology*, 3, 12 2020.

[15] Dagan Feng, Sung-Cheng Huang, and Xinmin Wang. Models for computer simulation studies of input functions for tracer kinetic modeling with positron emission tomography. *International Journal of Bio-Medical Computing*, 32:95–110, 3 1993.

[16] Peter T. Fox, Marcus E. Raichle, Mark A. Mintun, and Carmen Dence. Nonoxidative glucose consumption during focal physiologic neural activity. *Science*, 241:462–464, 7 1988.

[17] K. J. Friston, L. Harrison, and W. Penny. Dynamic causal modelling. *NeuroImage*, 19:1273–1302, 8 2003.

[18] Matthew F. Glasser, Stamatios N. Sotiropoulos, J. Anthony Wilson, Timothy S. Coalson, Bruce Fischl, Jesper L. Andersson, Junqian Xu, Saad Jbabdi, Matthew Webster, Jonathan R. Polimeni, David C. Van Essen, and Mark Jenkinson. The minimal preprocessing pipelines for the Human Connectome Project. *NeuroImage*, 80:105–124, 10 2013.

[19] Evan M. Gordon, Timothy O. Laumann, Babatunde Adeyemo, Jeremy F. Huckins, William M. Kelley, and Steven E. Petersen. Generation and evaluation of a cortical area parcellation from resting-state correlations. *Cerebral Cortex*, 26:288–303, 1 2016.

[20] Koen V. Haak, Andre F. Marquand, and Christian F. Beckmann. Connectopic mapping with resting-state fMRI. *NeuroImage*, 170:83–94, 4 2018.

[21] Robert Hall. Vascular injuries resulting from arterial puncture or catheterization. *British Journal of Surgery*, 58:513–516, 12 2005.

[22] Seok Jun Hong, Ting Xu, Aki Nikolaidis, Jonathan Smallwood, Daniel S. Margulies, Boris Bernhardt, Joshua Vogelstein, and Michael P. Milham. Toward a connectivity gradient-based framework for reproducible biomarker discovery. *NeuroImage*, 223, 12 2020.

[23] H.M. Hudson and R.S. Larkin. Accelerated image reconstruction using ordered subsets of projection data. *IEEE Transactions on Medical Imaging*, 13:601–609, 1994.

[24] M Jenkinson. Improved optimization for the robust and accurate linear registration and motion correction of brain images. *NeuroImage*, 17:825–841, 10 2002.

[25] Tim Jerman, Franjo Pernus, Bostjan Likar, and Ziga Spiclin. Enhancement of vascular structures in 3D and 2D Angiographic Images. *IEEE Transactions on Medical Imaging*, 35:2107–2118, 9 2016.

[26] Julia W Y Kam, Jack J Lin, Anne-Kristin Solbakk, Tor Endestad, Pål G Larsson, and Robert T Knight. Default network and frontoparietal control network theta connectivity supports internal attention. *Nature Human Behaviour*, 3:1263, 2019.

[27] Dong Soo Lee, Hyejin Kang, Heejung Kim, Hyojin Park, Jungsu S. Oh, Jae Sung Lee, and Myung Chul Lee. Metabolic connectivity by interregional correlation analysis using statistical parametric mapping (SPM) and FDG brain PET; methodological development and patterns of metabolic connectivity in adults. *European Journal of Nuclear Medicine and Molecular Imaging*, 35:1681–1691, 9 2008.

[28] Ai-Ling Lin, Peter T. Fox, Jean Hardies, Timothy Q. Duong, and Jia-Hong Gao. Nonlinear coupling between cerebral blood flow, oxygen consumption, and ATP production in human visual cortex. *Proceedings of the National Academy of Sciences*, 107:8446–8451, 5 2010.

[29] Pierre J. Magistretti and Igor Allaman. A cellular perspective on brain energy metabolism and functional imaging, 5 2015.

[30] Daniel S. Marcus, John Harwell, Timothy Olsen, Michael Hodge, Matthew F. Glasser, Fred Prior, Mark Jenkinson, Timothy Laumann, Sandra W. Curtiss, and David C. Van Essen. Informatics and Data Mining Tools and Strategies for the Human Connectome Project. *Frontiers in Neuroinformatics*, 5, 2011.

[31] Daniel S. Margulies, Satrajit S. Ghosh, Alexandros Goulas, Marcel Falkiewicz, Julia M. Huntenburg, Georg Langs, Gleb Bezgin, Simon B. Eickhoff, F. Xavier Castellanos, Michael Petrides, Elizabeth Jefferies, and Jonathan Smallwood. Situating the default-mode network along a principal gradient of macroscale cortical organization. *Proceedings of the National Academy of Sciences of the United States of America*, 113:12574–12579, 11 2016.

[32] Paul M. Matthews, Eugenii A. Rabiner, Jan Passchier, and Roger N. Gunn. Positron emission tomography molecular imaging for drug development. *British Journal of Clinical Pharmacology*, 73:175–186, 2 2012.

[33] M. Mesulam. From sensation to cognition. *Brain*, 121:1013–1052, 6 1998.

[34] Andrew C. Murphy, Maxwell A. Bertolero, Lia Papadopoulos, David M. Lydon-Staley, and Danielle S. Bassett. Multimodal network dynamics underpinning working memory. *Nature Communications*, 11:3035, 12 2020.

[35] S Ogawa, T M Lee, A R Kay, and D W Tank. Brain magnetic resonance imaging with contrast dependent on blood oxygenation. *Proceedings of the National Academy of Sciences*, 87:9868–9872, 12 1990.

[36] Casey Paquola, Reinder Vos De Wael, Konrad Wagstyl, Richard A.I. Bethlehem, Seok Jun Hong, Jakob Seidlitz, Edward T. Bullmore, Alan C. Evans, Bratislav Misic, Daniel S. Margulies, Jonathan Smallwood, and Boris C. Bernhardt. Microstructural and functional gradients are increasingly dissociated in transmodal cortices. *PLoS Biology*, 17, 5 2019.

[37] Brian Patenaude, Stephen M. Smith, David N. Kennedy, and Mark Jenkinson. A bayesian model of shape and appearance for subcortical brain segmentation. *NeuroImage*, 56:907–922, 6 2011.

[38] Clifford S. Patlak, Ronald G. Blasberg, and Joseph D. Fenstermacher. Graphical evaluation of blood-to-brain transfer constants from multiple-time uptake data. *Journal of Cerebral Blood Flow and Metabolism*, 3:1–7, 3 1983.

[39] L. Pellerin and P. J. Magistretti. Glutamate uptake into astrocytes stimulates aerobic glycolysis: a mechanism coupling neuronal activity to glucose utilization. *Proceedings of the National Academy of Sciences*, 91:10625–10629, 10 1994.

[40] Denis Peruzzo, Alessandra Bertoldo, Francesca Zanderigo, and Claudio Cobelli. Automatic selection of arterial input function on dynamic contrast-enhanced mr images. *Computer Methods and Programs in Biomedicine*, 104, 12 2011.

[41] M. E. Phelps, S. C. Huang, E. J. Hoffman, C. Selin, L. Sokoloff, and D. E. Kuhl. Tomographic measurement of local cerebral glucose metabolic rate in humans with (F-18)2-fluoro-2-deoxy-D-glucose: Validation of method. *Annals of Neurology*, 6:371–388, 11 1979.

[42] Alexander Schaefer, Ru Kong, Evan M Gordon, Timothy O Laumann, Xi-Nian Zuo, Avram J Holmes, Simon B Eickhoff, and B T Thomas Yeo. Local-Global Parcellation of the Human Cerebral Cortex from Intrinsic Functional Connectivity MRI. *Cerebral Cortex*, 28:3095–3114, 9 2018.

[43] R. Schofield, L. King, U. Tayal, I. Castellano, J. Stirrup, F. Pontana, J. Earls, and E. Nicol. Image reconstruction: Part 1 – understanding filtered back projection, noise and image acquisition. *Journal of Cardiovascular Computed Tomography*, 14:219–225, 5 2020.

[44] Gordon L. Shulman, Julie A. Fiez, Maurizio Corbetta, Randy L. Buckner, Francis M. Miezin, Marcus E. Raichle, and Steven E. Petersen. Common Blood Flow Changes across Visual Tasks: II. Decreases in Cerebral Cortex. *Journal of Cognitive Neuroscience*, 9:648–663, 10 1997.

[45] Erica Silvestri*, Tommaso Volpi*, Andrea Bettinelli, Mattia De Francisci, Judson Jones, Maurizio Corbetta, Diego Cecchin, and Alessandra Bertoldo. Image-derived Input Function in brain [18F]FDG PET data: which alternatives to the carotid siphons? *44th Annual International Conference of the IEEE Engineering in Medicine and Biology Society*, 2022, [Accepted].

[46] Abraham Z. Snyder and Marcus E. Raichle. A brief history of the resting state: The Washington University perspective. *NeuroImage*, 62:902–910, 8 2012.

[47] L. Sokoloff, M. Reivich, C. Kennedy, M. H. Des Rosiers, C. S. Patlak, K. D. Pettigrew, O. Sakurada, and M. Shinohara. The [14C]Deoxyglucose method for the measurement of local cerebral glucose utilization: Theory, procedure, and normal values in the conscious and anesthetized albino rat. *Journal of Neurochemistry*, 28:897–916, 5 1977.

[48] Louis Sokoloff, Renward Mangold, Richard L. Wechsler, Charles Kennedy, and Seymour S. Kety. The effect of mental arithmetic on cerebral circulation and metabolism 1. *Journal of Clinical Investigation*, 34:1101–1108, 7 1955.

[49] Lalith K.S. Sundar, Otto Muzik, Lucas Rischka, Andreas Hahn, Ivo Rausch, Rupert Lanzenberger, Marius Hienert, Eva Maria Klebermass, Frank Günther Füchsel, Marcus Hacker, Magdalena Pilz, Ekaterina

Pataraia, Tatjana Traub-Weidinger, and Thomas Beyer. Towards quantitative [18F]FDG-PET/MRI of the brain: Automated MR-driven calculation of an image-derived input function for the non-invasive determination of cerebral glucose metabolic rates. *Journal of Cerebral Blood Flow and Metabolism*, 39:1516–1530, 8 2019.

[50] Ye Tian, Daniel S. Margulies, Michael Breakspear, and Andrew Zalesky. Topographic organization of the human subcortex unveiled with functional connectivity gradients. *Nature Neuroscience*, 23:1421–1432, 11 2020.

[51] Dardo Tomasi, Gene Jack Wang, and Nora D. Volkow. Energetic cost of brain functional connectivity. *Proceedings of the National Academy of Sciences of the United States of America*, 110:13642–13647, 8 2013.

[52] Dardo G Tomasi, Ehsan Shokri-Kojori, Corinde E Wiers, Sunny W Kim, Şukru B Demiral, Elizabeth A Cabrera, Elsa Lindgren, Gregg Miller, Gene-Jack Wang, and Nora D Volkow. Dynamic brain glucose metabolism identifies anti-correlated cortical-cerebellar networks at rest. *Journal of Cerebral Blood Flow and Metabolism*, 37:3659–3670, 12 2017.

[53] Matteo Tonietto, Gaia Rizzo, Mattia Veronese, and Alessandra Bertoldo. Modelling arterial input functions in positron emission tomography dynamic studies. pages 2247–2250. IEEE, 8 2015.

[54] Matteo Tonietto, Gaia Rizzo, Mattia Veronese, Masahiro Fujita, Sami S. Zoghbi, Paolo Zanotti-Fregonara, and Alessandra Bertoldo. Plasma radiometabolite correction in dynamic PET studies: Insights on the available modeling approaches. *Journal of Cerebral Blood Flow and Metabolism*, 36:326–339, 2 2016.

[55] Lucina Q. Uddin, B. T.Thomas Yeo, and R. Nathan Spreng. Towards a universal taxonomy of macro-scale functional human brain networks, 11 2019.

[56] Mattia Veronese, Roger N. Gunn, Stefano Zamuner, and Alessandra Bertoldo. A non-linear mixed effect modelling approach for metabolite correction of the arterial input function in PET studies. *NeuroImage*, 66:611–622, 2 2013.

[57] Mattia Veronese, Lucia Moro, Marco Arcolin, Ottavia Dipasquale, Gaia Rizzo, Paul Expert, Wasim Khan, Patrick M. Fisher, Claus Svarer, Alessandra Bertoldo, Oliver Howes, and Federico E. Turkheimer. Covariance statistics and network analysis of brain pet imaging studies. *Scientific Reports*, 9, 12 2019.

[58] Tommaso Volpi, John J. Lee, Erica Silvestri, Tony Durbin, Maurizio Corbetta, Manu S. Goyal, Andrei G. Vlassenko, and Alessandra Bertoldo. Modeling venous plasma samples in [18F]FDG PET studies: a nonlinear mixed-effects approach. *44th Annual International Conference of the IEEE Engineering in Medicine and Biology Society*, 2022,[Accepted].

[59] Tommaso Volpi, Erica Silvestri, Maurizio Corbetta, and Alessandra Bertoldo. Assessing different approaches to estimate single-subject metabolic connectivity from dynamic [18F]fluorodeoxyglucose. *2021 43rd Annual International Conference of the IEEE Engineering in Medicine & Biology Society (EMBC)*, pages 3259–3262, 11.

[60] Igor Yakushev, Alexander Drzezga, and Christian Habeck. Metabolic connectivity: methods and applications. *Current Opinion in Neurology*, 30:677–685, 12 2017.

[61] B. T. Thomas Yeo, Fenna M. Krienen, Jorge Sepulcre, Mert R. Sabuncu, Danial Lashkari, Marisa Hollinshead, Joshua L. Roffman, Jordan W. Smoller, Lilla Zöllei, Jonathan R. Polimeni, Bruce Fischl, Hesheng Liu, and Randy L. Buckner. The organization of the human cerebral cortex estimated by intrinsic functional connectivity. *Journal of Neurophysiology*, 106:1125–1165, 9 2011.

[62] Yufeng Zang, Tianzi Jiang, Yingli Lu, Yong He, and Lixia Tian. Regional homogeneity approach to fmri data analysis. *NeuroImage*, 22:394–400, 5 2004.

[63] Paolo Zanotti-Fregonara, Kewei Chen, Jeih-San Liow, Masahiro Fujita, and Robert B Innis. Image-derived input function for brain pet studies: Many challenges and few opportunities. *Journal of Cerebral Blood Flow and Metabolism*, 31:1986–1998, 10 2011.

[64] Paolo Zanotti-Fregonara, El Mostafa Fadaili, Renaud Maroy, Claude Comtat, Antoine Souloumiac, Sebastien Jan, Maria-Joao Ribeiro, Véronique Gaura, Avner Bar-Hen, and Régine Trébossen. Comparison of Eight Methods for the Estimation of the Image-Derived Input Function in Dynamic [18F]-FDG PET Human Brain Studies. *Journal of Cerebral Blood Flow and Metabolism*, 29:1825–1835, 11 2009.